Subsurface molecular bubbles: the ignored interfacial degradation factor of LIBs graphite anode

Yue Chen [a, b, c 1], Wenye Xuan [d, e 1], Weijian Zhang [a, f], Nagarathinam, Mangayarkarasi [b, c], Shaohua Zhang [a, f], Jianming Tao [a, g], Jiaxin Li [a, f], Long Zhang [a], Yingbin Lin* [a, f], Yubiao Niu [h], Hsin-Yi Tiffany Chen* [e], Svetlana Menkin Bachbut [b, i], Dominic Wright [b, i], Clare P. Grey [b, i], Oleg V. Kolosov* [b, c] and Zhigao Huang* [a, g]

[a] College of Physics and Energy, Fujian Normal University, Fujian Provincial Key Laboratory of Quantum Manipulation and New Energy Materials, Fuzhou 350117, China

[b] The Faraday Institution, Quad One, Harwell Science and Innovation Campus, Didcot OX11 0RA, UK

[c] Department of Physics, Lancaster University, Lancaster LA1 4YB, UK

[d] Department of Chemistry, University of Liverpool, Liverpool L69 7ZD, UK

[e] Department of Engineering and System Science, National Tsing Hua University, Hsinchu 30013, Taiwan

[f] Fujian Provincial Engineering Technical Research Centre of Solar-Energy Conversion and Stored Energy, Fuzhou 350117, China

[g] Fujian Provincial Collaborative Innovation Centre for Advanced High-Field Superconducting Materials and Engineering, Fuzhou 350117, China

[h] We Are Nium Ltd. Research Complex at Harwell (RCaH), Rutherford Appleton Laboratory, Harwell, Didcot OX11 0FA, UK

[i] Yusuf Hamied Department of Chemistry, University of Cambridge, Lensfield Road, Cambridge CB2 1EW, UK

Corresponding authors: *yblin@fjnu.edu.cn, hsinyi.tiffany.chen@gapp.nthu.edu.tw, o.kolosov@lancaster.ac.uk, zghuang@fjnu.edu.cn

[1]Y. C. and [1]W. X. contributes equally

Abstract

The interplay between solvent co-intercalation, solid-electrolyte-interphase (SEI) formation and gas evolution on graphite anode-electrolyte interface has not yet been explicitly explored at nanoscale. In this work, *operando* atomic force microscopy (AFM), combining with novel ultrasonic excitation, was introduced to visualize the nanoscale interrelated solvent co-intercalation, SEI formation, as well as the subsurface gas evolution in graphite anode for lithium-ion batteries. Interestingly, we found that the subsurface gas evolution results in the "molecular bubbles" trapped between carbon layers, which were designated as a previously ignored interfacial degradation factor during formation cycles. The solvent co-intercalation and decomposition, which were found to be the two preconditions of molecular bubble-induced interfacial degradations, can be suppressed through optimizing the intermolecular interaction by adding fluorobenzene as the non-solvating diluent solvent. The force-distance spectroscopy and modelling results reveal that, the chemically inert fluorobenzene molecule, preferentially adsorbing on the graphite-anode surface, acts as an interfacial protection layer between the localized lithium-solvation clusters and graphite surface, effectively enhancing the graphite-electrolyte interfacial stability.

Introduction

The conventional formation process of commercial lithium/sodium ion batteries (LIBs/SIBs) requires low-rate charge/discharge cycles to form a mechanical robust and chemical uniform solid-state interphase (SEI) layer[1,2]. During the formation cycles of graphite anode, the electrolyte decomposition generates not only the protective SEI layer but also the bootless gas products that can damage the integrity of the SEI layer[3]. To accelerate the SEI formation and minimize the gas evolution-induced interfacial structural degradations, a deeper understanding of interfacial chemistry during the formation is urgently required.

The formation of SEI and gas evolution in graphite anodes are closely interrelated interfacial phenomena. The SEI layer is a result of electrolyte decomposition which forms a passivating film that separates the reactive electrode from the electrolyte[4]. Gas evolution, on the other hand, is often associated with the decomposition of the electrolyte and the subsequent reactions occurring at the graphite-electrolyte interface[3,5]. The SEI layer formation often involves the generation of gases, such as carbon dioxide and hydrocarbons[6-8]. In turn, the gas evolution can affect the formation and stability of the SEI layer, causing uneven ion transportation at interfaces[3,9] and ultimately leading to diminished shelf life and battery lifetime.

So far, various measures, such as electrolyte additives, surface modification, and electrode engineering are being explored to enhance the stability of the SEI layer and mitigate gas evolution in graphite anodes[5,10-12]. However, when it comes to interfacial structural degradations, often, the gas evolution on graphite-electrolyte interface[13,14] is overlooked. It is intuitively reasonable to assume that, the gases generated at the edge planes of graphite are able to diffuse into both the graphite interlayers and liquid electrolyte. The gas released into the electrolyte, forming macroscale bubbles inside the battery pouches, has extensively been studied by chromatography mass spectrometer[15], X-ray tomography[16], neutron radiography[17] and ultrasonic scanning machines[18,19]. In contrast, the gas evolutions on electrochemical solid-liquid interface and released into the graphite may also induce nano-bubbles trapped inside solid lattice[20,21], which are rarely explored and still far from fully understood due to the lack of nanoscale solid-liquid interface characterization techniques. One example is the nano bumps observed on the carbon anode surface, which were previously interpreted as the nanoblisters[22,23] filled by co-intercalated liquid solvent between the carbon layers. Another example is oxygen redox in cathode lattice,[24] which has raised more and more research interests, yet it is still hard to experimentally detect and studied at nanoscale[25,26]. The giant difference in the acoustic permeability/ transmittance of gas, liquid and solid phases inspires us to deploy the electrochemical ultrasonic force microscopy[27-29] (EC-UFM) to study the nanoscale gas evolution behaviour, *in situ* and *operando*, on battery interfaces.

Thanks to the non-invasive and non-destructive characteristics of ultrasound, ultrasound-based techniques enable *in situ*/*operando* monitoring of gas evolution without disrupting the internal structure of the battery[30-33]. These ultrasound-based techniques exhibit high sensitivity to changes in the physical and chemical properties of materials inside the battery package, allowing for the detection of small variations and transient gas evolution behaviours, as well as the identification of potential issues or abnormalities within the battery. However, current ultrasound-based characterization techniques, such as the ultrasound-based 2D imaging method[30], merely allowing for the millimetre-scale localization of gas evolution within the pouch cell[31]. The nanostructures of the graphite-electrolyte interface during the gas evolutions, which can restrict the comprehensive understanding of macroscale gas evolution processes throughout the entire battery structure, still cannot accessed by these ultrasound techniques.

In this work, we introduced a novel ultrasound-based atomic force microscopy (Supplementary notes 1 and 2) to study the complicated interrelations of SEI formation and gas evolution on the graphite-electrolyte interface at the nanoscale. Few-layer graphene atomic steps were used as the ideal model. Subsurface molecular bubbles trapped inside the graphene interlayer were observed and attributed to the interfacial structural degradation during the formation. Solvent co-intercalation and decomposition between the carbon interlayers are found to be the main causes of subsurface molecule bubble formation. To inhibit these interfacial degradations, we tune the electrolyte component by adjusting the dipole-dipole interactions using non-solvation diluent, and then dig into the deep insights of intermolecular interaction and interfacial electrolyte structures of our optimized electrolytes. The optimized electrolyte enables the negligible formation of subsurface molecular bubbles and SEI layer, and the non-destructive graphite-electrolyte interface improve the cycle stability and columbic efficiency of cell under an elevated formation current density.

Main

1. Macroscale and nanoscale interfacial degradations during galvanostatic formations

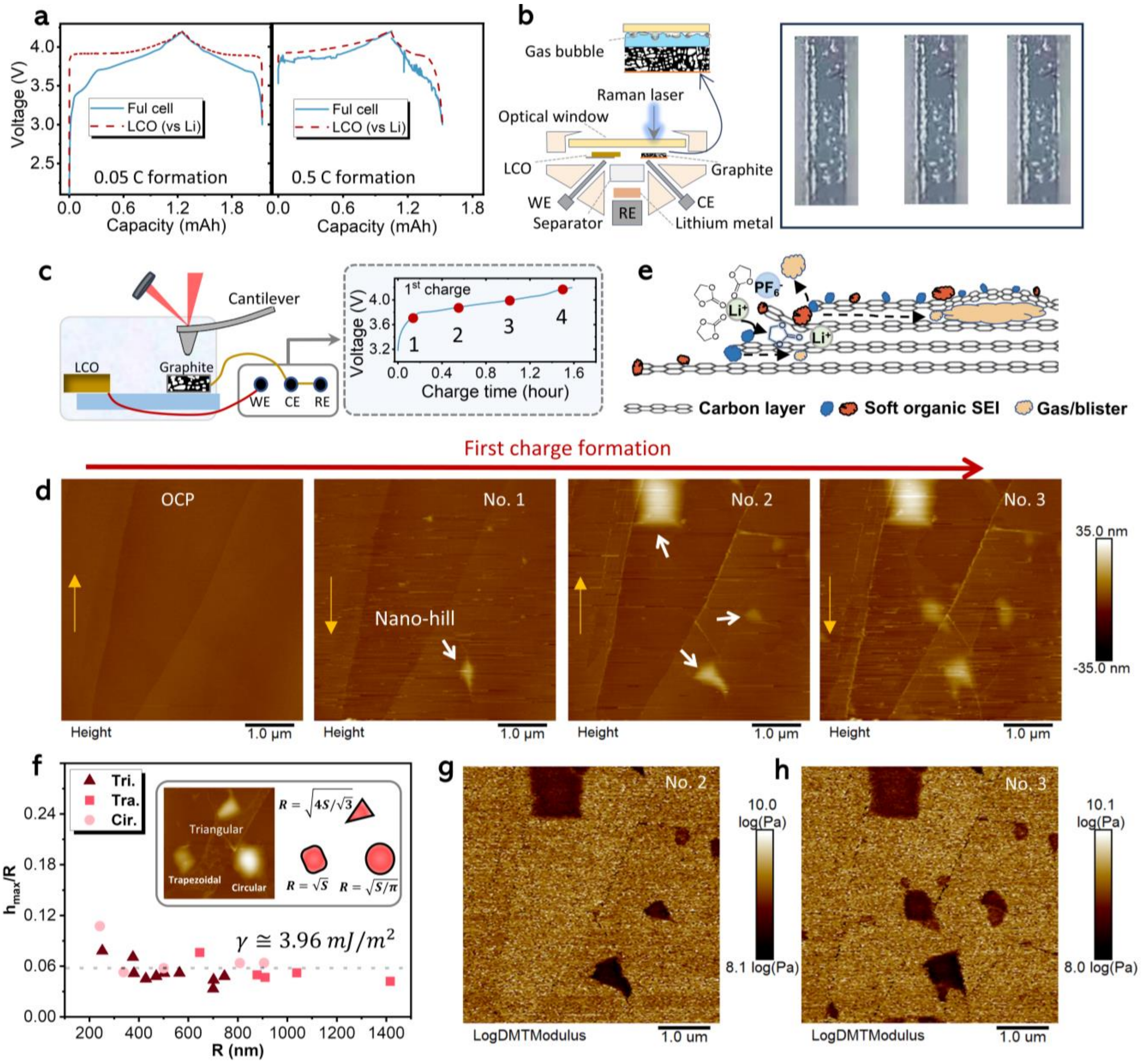

Figure 1 Macroscale and nanoscale interfacial structural degradation of graphite anode during the initial galvanostatic formation in 1 M $LiPF_6$ in EC: DEC=1:1 v%. (a) The formation charge and discharge curves of $LiCoO_2$//Graphite full cell in three-electrode geometry. The blue solid lines are the full cell voltage; the red dashed lines are the $LiCoO_2$ cathode voltage. (b) Schematic diagram of an electrochemical cell for *operando* optical microscopy. (Supplementary Information (SI), Figure 1) (c) Schematic diagram of graphite anode measured by conventional electrochemical atomic force microscopy (EC-AFM) during the formation charging (~0.63 C). The galvanostatic charge curves are shown beside the diagram. (d) Surface topography changes of graphite anode observed by *operando* EC-AFM during the lithiation at different charge states No. 1-4 as denoted in Figure 1c. The video of *operando* scanning observation in supplementary, VIDEO-1 (e) Schematic diagram of the "nano-hills" and SEIs formed on graphite anode surface. (f) The statistic results of the maximum height *vs* radium ratio of the nano-hills. The effective radius R determined as $R = \sqrt{S/\pi}$, $R = \sqrt{S}$ and $R = \sqrt{4S/\sqrt{3}}$ for circular, trapezoidal and triangular nano-hills, respectively. (h) The mechanical modulus images of the nano-hills at charge stages No. 2 and No. 3 in Figure 1d.

Figure 1a shows the galvanostatic charge/discharge curves of a $LiCoO_2$//Graphite full cell (solid blue lines) and the $LiCoO_2$ cathode (red dashed lines) using a three-electrode test cell under a current density of 0.05 C and 0.5 C. At large formation current density, the serious fluctuations of full-cell charge/discharge curve and decreased reversible capacity are observed. By contrast, the cathode voltage curve stays smooth and stable, indicating the formation rate of full-cell is limited by the graphite anode[34,35]. According to the optical microscopy observations (Figure 1b), this capacity degradation on the anode side can be partially attributed to the gas evolution on the graphite anode surface (Supplementary information, SI, Figure 1). The gas products accumulated on the graphite-electrolyte interface separate the active lithium storage sites and electrolyte, leaving a large proportional of graphite particles not fully lithiated into LiC_6 (see Raman spectroscopy in SI, Figure 2a). Therefore, the macroscale gas evolution and accumulation on graphite-anode interface was found to be the "visible" cause of capacity degradations during the battery formation.

Operando EC-AFM (Figure 1c) was used to further study the nanoscale "invisible" interfacial degradation processes on graphite anode surface. As shown in Figure 1d, the surface morphology evolutions of basal planes on a graphite particle surface are observed by EC-AFM at open circuit potential (OCP) and different charging voltages (No. 1-4). Surprisingly, we observed the nucleation and growth of many "nano-hills" during the galvanostatic charging. The first nano-hill appears on the nanoscale flat graphite surface at voltage region No. 1, after which the size of nano-hill increases with the lithium-ion intercalating into the graphite atomic steps. At the end of charge, not only the nano-hills were formed on the anode surface, but also the SEI nanoparticles sporadically covering the graphite surface (see AFM image at voltage region No. 4 in SI, Figure 2b and 2c). As schemed in Figure 1e, these nano-hills are no doubt a result of local delamination, similar to the previously reported gas bubbles or liquid blisters trapped by many 2D materials[36,37]. Figure 1g shows the statistical value of the maximum height *vs* radium (h_{max}/R) ratio of the nano-hills with different shapes. The aspect ratio (h_{max}/R) of the nano-hills is determined by the total adhesion energies γ by[38]

$$\frac{h_{max}}{R} = \left(\frac{\pi\gamma}{3.5Y}\right)^{1/4} \qquad (1)$$

Where Y is the Young's modulus of graphene, R is the reduced radium of nano-hill and total adhesion energy γ is related to the vdW force between graphene and the substrate[36], as well as the gas/liquid substance trapped inside the nano-hills[38,39] (see supplementary note 3). The average h_{max}/R value is around 0.06, suggesting the adhesion energy (~4.91 mJ/m^2) of the graphene nano-hill system is quite small. This adhesion energy value and aspect ratio are close to the previously reported H_2/O_2 bubble trapped by graphene[21,40], implying trapped substances inside the carbon layers are the gases. The dynamic evolutions of nano-mechanical properties of nano-hills were further determined by DMT modulus measurements (SI, VIDEO-1). As shown in Figures 1h and 1i, the nano-hills show a much darker contrast compared with the graphite (001) plane, having a DMT modulus at around $10^{8\text{-}9}$ Pa. Although the pressure induced by the nano-hills is neither large enough to break the flexible graphene[41] nor large enough to liquify the trapped gases[42], these "invisible" nano-hills may block the ion transport through the electrode-electrolyte interface. Overall, apart from the "visible" macroscale bubble accumulations in electrolytes, EC-AFM measurements confirmed that the nano-hills formation is the other important, but previously ignored "invisible" interfacial degradation mechanism.

2. Interrelated SEI and nano-hill formations: nano blister or bubble?

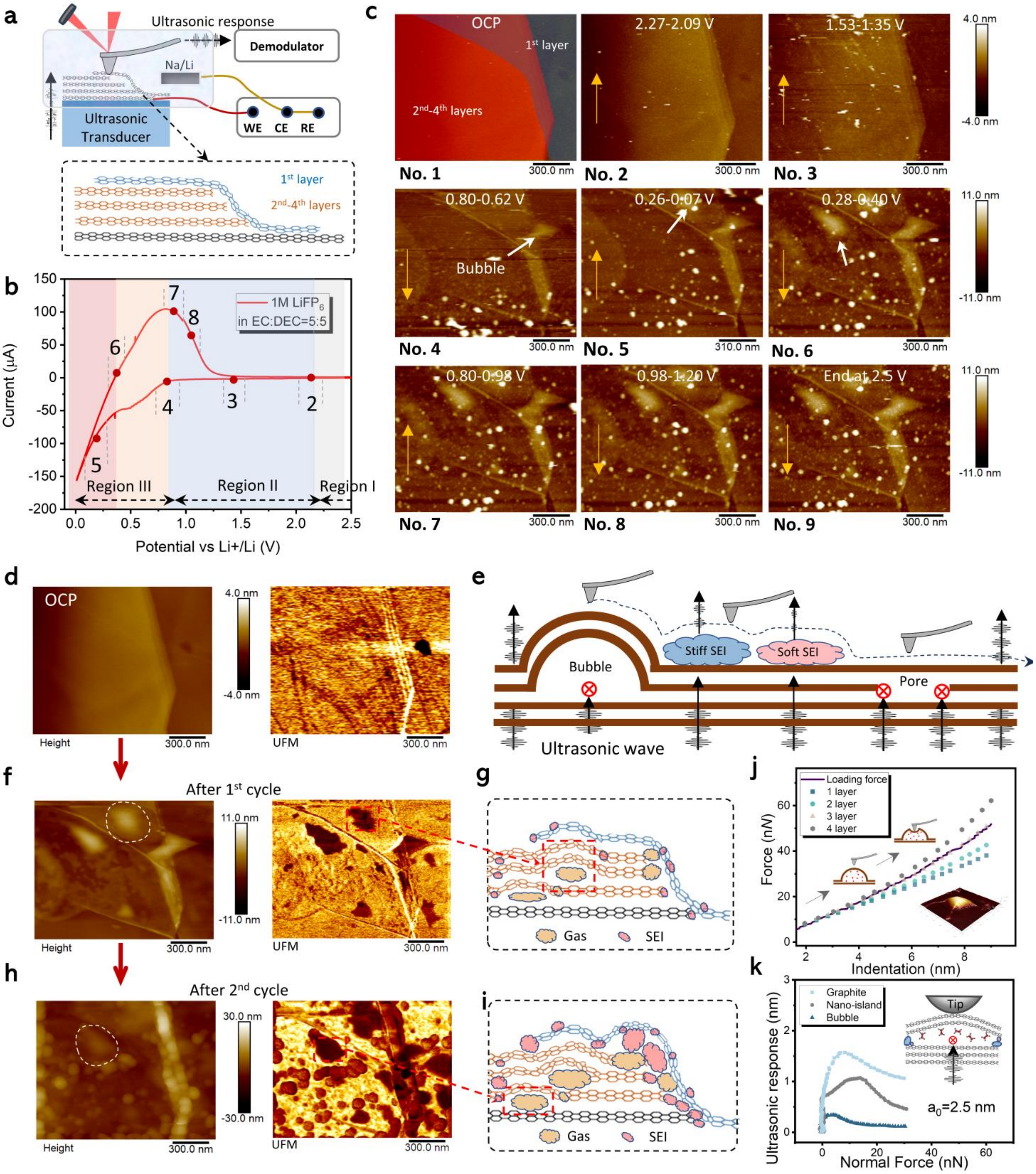

Figure 2 Nanoscale SEI formation and gas evolution observed by *operando* EC-AFM and *in situ* ultrasonic force microscopy (UFM). (a) Schematic diagram of electrochemical AFM combined with an ultrasonic wave excitation. The graphite model sample consists of four overlapped carbon layers. (b) The cyclic voltammetry (CV) curve of AFM EC-cell during the first lithiation in 1 M $LiPF_6$ in EC: DEC=1:1 v%. (c) Surface topography changes of graphite atomic steps during the first lithiation. The first top carbon layer and the second to fourth carbon layers are labelled in blue and red in Figure 2c, No. 1. The images at different lithiation/de-lithiation states (denoted as voltage regions No. 1-9) correspond to the point in the voltage curve in Figure 2c. (d) Surface topography and UFM images at open circuit potential (OCP) before CV cycles. (e) Schematic of ultrasonic waves transport through different

components. (f) The surface topography and UFM images after the 1st cycle and (h) the 2nd cycle, and their nanobubble trapping models (g) and (i). (j) Force indentation curve (dark curve) of graphene bubble and corresponding numerical fits (dots) by different 2D Young's Modulus values. (k) Ultrasonic force spectroscopy (UFS) (supplementary note 2) of the bubbles, SEI components and graphite substrate.

To understand the interrelated SEI and nano-hills formations, we further observed the surface topography evolutions of a few-layer carbon atomic step (SI, Figure 3) upon the lithiation/delithiation at different voltages using cyclic voltammetry (CV) (Figure 2a). The EC-AFM are operated in peak-force QNM mode[43] to record the surface topography, and in UFM mode[44] to detect the subsurface structures, respectively. The principle and technical details of ultrasonic-based microscopy can be found in the supplementary note 1.

Figure 2b is the 1st CV in 1 M $LiPF_6$ in EC: DEC=1:1 v%, the voltage range can be divided into three different regions according to the different electrochemical processes that occur on the graphite surface. In region I (OCP→~2.25 V), the cathodic current stays constant at < 1 µA (SI, Figure 4), indicating that the electrode surface is located within the thermodynamically stable voltage window. When entering the voltage region II, the typical surface topography image recorded between 2.27-2.09 V can be found in Figure 2c, very scattered SEI nanoparticles (white spots) start to appear on the graphite basal plane. With voltage scanning down to about 1.35 V, the cathodic current increases by three times. Meanwhile, more irregular nanoparticles that may attributed to the LiF [2] start to form on the graphite basal plane[2] (Figure 1c, No. 3). However, the carbon atomic step height remains constant at around 1.01 nm (SI, Figure 3), indicating that massive intercalation has not yet occurred in this voltage region (2.25-1.35 V). Interestingly, significant topography changes happen when the electrode voltage reaches voltage region III, in which many dense nanoparticles fully cover the electrode surface and the carbon step height increases to about 1.55 nm (SI, Figure 3) due to the solvent co-intercalation. Moreover, the first nano-hill formed in the measured area (Figure 1c, No. 4) was also observed at this voltage region. Upon the following measurements (Figures 2c, No. 5 and No. 6), the SEI nanoparticles with bigger size and more nano-hills keeps forming on the electrode surface until the electrode current changed from cathodic current to anodic current. But the surface morphology and nano-hill size stay relatively unchanged from the anodic scan to the end of the CV cycle (Figure 2c, No. 7-9), indicating the nano-hills formation is a cooccurrence phenomenon with SEI formations (electrolyte reductive decompositions) and lithium co-intercalations.

We further introduced UFM to explore the subsurface substance inside the nano-hills. By applying the ultrasonic excitation (~4 MHz) with an amplitude of a few angstrom meters from the bottom of the electrode, and detecting the localized nanoscale ultrasonic response on the electrode surface during the nano-tip scanning. The obtained UFM image can provide the contrast of ultrasonic permeability and mechanical stiffness (Supplementary note 2) at each scanning pixel on the topography image as shown in Figures 2d-i. Figure 2d shows the topography and UFM image of carbon steps before the CV cycles, the native subsurface dislocations[27] and a pore, buried underneath the top carbon layer, appear in the UFM image as dark lines and circles, respectively. As shown in Figure 2e, the pore (gas bubble) is a bad propagation medium for ultrasonic waves, and it will “block” the ultrasonic excitation coming from the substrate and therefore appear as dark UFM contrast. Figures 2f and 2h are the UFM measurements of the carbon step after the 1st and 2nd CV cycles (also see SI, Figure 5 for the DMT modulus). The soft SEI was scratched by AFM tip before the UFM measurements (SI, Figure 6). In Figure 2f, the nano-hill (in white dashed circles) in topography present significantly low ultrasonic response in the UFM image. This indicates the space underneath these nano-hills have similar ultrasonic permittivity with the pore structure, indicating it is a gas-filled space that has a larger damping effect on the ultrasound vibration. Namely, these nano-hills are subsurface bubbles, rather than the blisters filled with liquid electrolyte.

The force-distance curves of the bubble region with vertical force modulation[45] and ultrasonic force modulation are shown in SI, Figures 7 and 8, in which one can find that the UFM response at the graphite region is about one order of magnitude larger than the UFM response at bubble region during the indentation. Moreover, as shown in Figure 2j, by fitting the vertical force during the indentation into the bubble[46] (SI, Figure 9 and Supplementary note 4), this bubble was suggested to be constrained by three carbon layers (between the 3rd and 4th layers) as illustrated in Figure 2g. After the 2nd lithiation/de-lithiation cycle, the sizes of bubbles trapped inside the carbon interlayers barely increased, while more round-shape “nano-islands” fully covered the graphite surface, especially accumulated on the step edges (Figure 2h). These nano-islands has smaller ultrasonic response compared with graphite, but larger than subsurface bubbles (SI, Figure 10). Ultrasonic force spectroscopy (UFS) measurements performed on the bubble, nano-island and graphite substrate areas are shown in Figure 2k. Under the ultrasonic excitation amplitude of 2.5 nm, the graphite substrate exhibits a maximum UFS response of about 1.60 nm, which is larger compared to the “nano-island” (~1.07 nm) and bubble areas (~0.35 nm). The mechanical modulus of nano-islands determined by UFS is at the order of about $10^{9\text{-}10}$ Pa (SI, Figure 11 and Supplementary note 2), close to the values of the reported inorganic SEI components[47-50]. Therefore, as sketched in Figure 2i, we attributed these round-shape islands accumulated on the graphite basal plane and the carbon step edge to the stiff inorganic SEIs that seal the entrances of solvent co-intercalation or the gas inner diffusion. As a result, the interface is becoming more inactive toward any electrolyte decomposition-induced structural changes, and then the subsurface bubbles stop growing.

3. Visualizing solvent co-intercalation: the “triggers” of initial subsurface bubble formations

Within the initial bubble formation voltage region (OCP-0.8 V), we study the nanostructural surface and subsurface evolutions of a few-layer carbon anode under the constant voltage polarizations. The AFM results are shown in Figure 3a. With the decrease of polarization voltage from OCP to 0.8 V, one can observe the curling of carbon step edges caused by the intercalations, as well as the nucleation of the “SEI seeds” on the surface. The step height of the triple-carbon layer increases from the initial value of about 0.99 nm (OCP) to 1.52 nm at 0.8 V (Figure 3b), indicating a co-intercalation of other species excepting lithium ions. The value of increased height is close to the diameter of the solvent molecule, rather than the lithium-solvent complex, unambiguously suggesting the co-intercalated solvents and lithium ions may stay in the de-solvation states inside the carbon layers. According to the Raman spectrum at each polarization voltage, the increasing of G peak intensity is also observed at polarization voltage 1.0 V and 0.8 V. The G peak slightly shifts to the higher wavenumber region, also indicating the increase of the force constants of the in-plane C–C bonds due to the lithium/solvent co-intercalation due to the formation of the dilute stage 1 graphite intercalation components (GICs)[51].

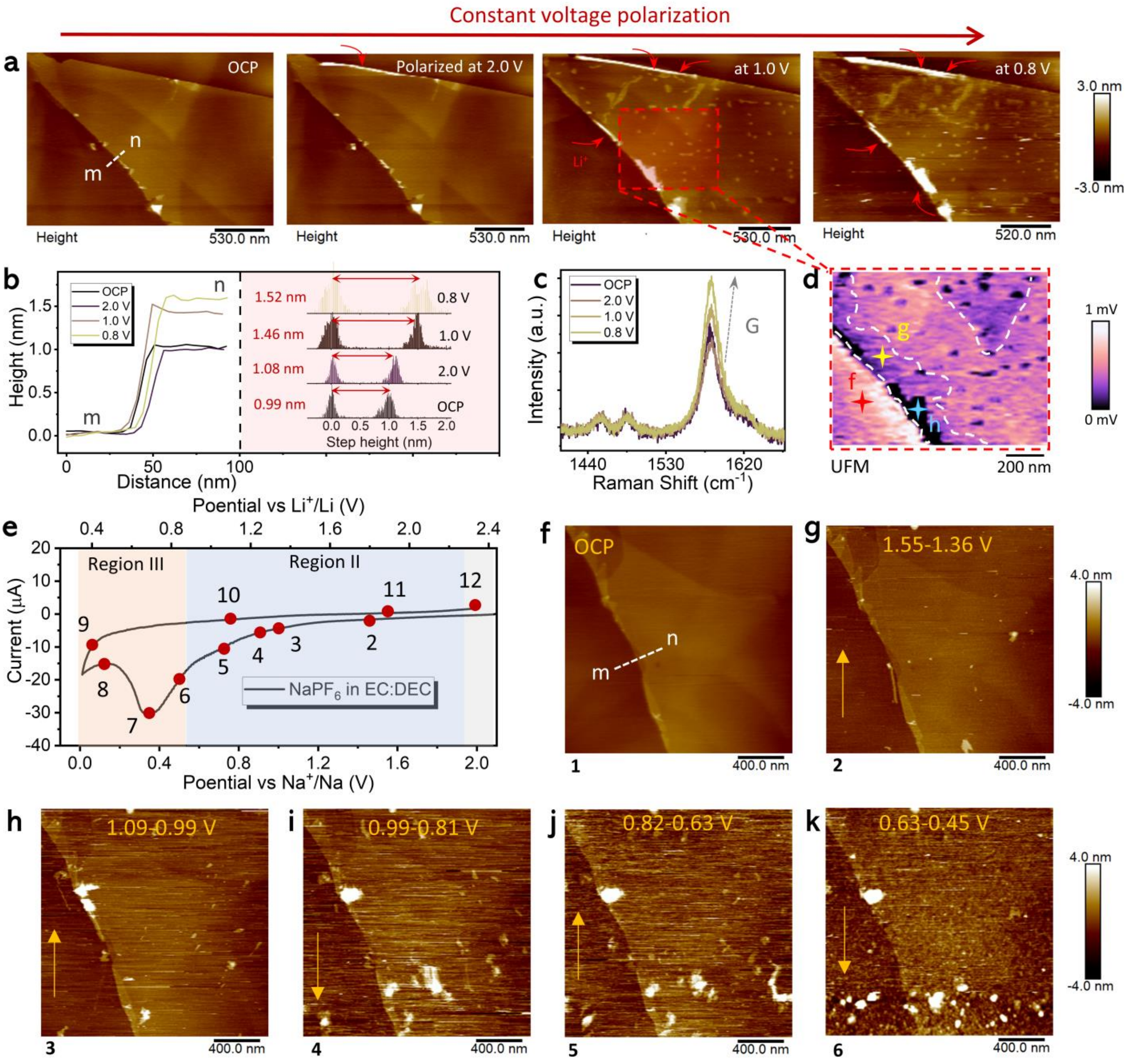

Figure 3 The initial stage of lithium/solvent co-intercalation and SEI formation revealed by UFM. (a) Surface topography of the graphite anode under the different polarization voltages. (b) Cross-section and histogram of the step height of carbon layers during the polarizations. (c) Raman spectra of graphite surface at each polarization voltage. (d) Zoom-in ultrasonic mapping on the few-layer graphite surface at polarization voltage of 1.0 V. (e) The 1st CV curve of few-layer carbon step anode cycled in $NaPF_6$ EC: DEC=1:1 electrolyte. The voltage regions II and III were labelled according to the CV curve in Figure 2c for comparison. (f-k) Surface topography evolutions during the 1st CV cycles. The number of each image corresponds to the number labelled in Figure 3e; the voltage in the images is the electrode voltage to the Na^+/Na.

The solvent co-intercalation was further resolved by UFM as shown in Figures 3d. The UFM image of the triple-layer graphene shows three different contrasts in the ultrasonic response mapping. Compared with the UFM image before the solvent co-intercalation (SI, Figure 12), we find an "electrolyte-immersed liked" region near the carbon step edges (as denoted by the white dashed line in Figure 3d). The ultrasound response inside the dashed-line area (Figure 3d) is larger than the SEI seeds but smaller than the graphite substrate. UFS with different excitation amplitudes were recorded at the typical graphite substrate region, electrolyte-immersed region and one of the carbon step edges at the points *f*, *g* and *h*, respectively, in Figure 3d. The UFS results are presented in SI, Figures 13. We found the UFS in the electrolyte-immersed region is weak, indicating a small slope of the force-indentation curve (supplementary note 2). This region can be attributed to the solvent co-intercalated GIC, which is softer than the original graphite due to the damping effects of the solvent molecules between carbon layers. Moreover, the UFS at the carbon step edge shows negligible signal, confirming the SEI/gas accumulated at the carbon edge forms a softer and lower acoustic permittivity region compared with GIC. Summarising, the solvent co-intercalation and decomposition were observed to occur at the very end of the graphite edge during the initial stage of SEI/bubble formation (at ~ 1 V vs Li^+/Li), which are the preconditions of subsurface molecular bubble formations.

A counter-example to support the correlation between the co-intercalation and subsurface molecular bubble is shown in Figures 3e-k, in which we replaced the cation from Li^+ to Na^+ (1 M $NaPF_6$ in EC: DEC=1:1 v%) and further evaluated the voltage-dependent electrochemical processes that occurred on a triple-layer carbon step (The video of *operando* scanning observation in supplementary, VIDEO-2). Figure 3e is the 1st CV curve during the first sodiation. Different from the CV curve in Figure 2c, the CV curve in Figure 3e only shows a reduction peak corresponding to the decomposition of the electrolyte, no oxidation peak was found upon the anodic scan, indicating that, the electrolyte decomposition does occur on the anode surface, but the sodium/solvent intercalation does not exist in this system. This reduction peak disappeared during the second cycle (SI, Figure 14). The surface topography images in Figures f-k revealed the onset of the SEI formation occurs at around 1.1 V, while the carbon atomic step height does not change (SI, Figure 15), and no step edge curls and SEI accumulation at the carbon atomic step were observed (SI, Figure 16). That is to say, if there is no cation/solvent co-intercalation, even when the electrode surface is polarized outside of the electrochemical stable window of the electrolyte, the subsurface bubble does not occur.

5. Understanding solvent co-intercalation and decomposition — effects of dipole-dipole interactions between free solvent and lithium-solvation complexes

Graphite-electrolyte interfacial degradation, either SEI or subsurface molecular bubble formations, is dedicated by the interfacial chemistry of lithium-solvation complexes, including the de-solvation, co-intercalation and decomposition. In the diluent (1M) commercial battery electrolyte, the molar ratio of solvent is about ten times higher than the cation and anode, therefore the dipole-dipole interactions in electrolytes play a significant role in optimizing the battery interfacial chemistry[52,53]. To understand and inhibit the interfacial degradation, we further study and evaluate the effects of intermolecular interactions between free solvent and lithium-solvation complexes in EC&DEC based electrolyte with and without diluent solvent.

Fourier transform infrared (FTIR) spectroscopy was used to understand the intermolecular interactions in 1M $LiPF_6$ in EC & DEC electrolytes with various EC: DEC ratios as shown in Figure 4a (full spectra can be found in SI, Figure 17). We observed a large proportion of solvated C-O band (~1302 cm^{-1}) of DEC, confirming the nonnegligible DEC molecules are participating in the solvation with Li^+[54]. With the increase of EC: DEC ratio, the blue shift of the C-O peak of free DEC (~1260 cm^{-1}) and solvated DEC (~1303 cm^{-1}) were also observed, which can be attributed to the enhanced dipole-dipole interaction with free EC molecules[53]. The C-H peak (~2990 cm^{-1}) of DEC blue shift with the increase of EC, meanwhile, the C=O peak (~1800 cm^{-1}) of free EC solvent blue shift with the decrease of DEC, indicating the existence of the molecular interaction between the C-H in DEC and C=O in free EC[53]. Interesting, we also noticed that these dipole-dipole interactions also exist in the pure EC mix DEC solvent (SI, Figure 18). Giving that the polarizing effect of Li^+ on the EC molecule can further enhance the diploe-diploe interactions between solvated EC molecular and free solvents[55], these dipole-dipole interactions was further taken into considerations for evaluating the chemical stability and de-solvation energy of lithium-solvation complexes using Density Functional Theory (DFT) modelling.

DFT modelling was used to find the “culprits” of the specific solvation complexes that trigger the solvent co-intercalation and decomposition. As shown in Figures 4c and 4d, we constructed the models with three types of Li-solvent complexes, $Li^+[EC_4]$, $Li^+[DEC_1EC_3]$ and $Li^+[DEC_2EC_2]$, absorbing on the graphite edge plane to evaluate their adsorption energies. The intermolecular interactions between the free solvents and lithium-solvation complexes were treated by implicit model through tuning the dielectric constant of the simulation system. The dielectric constants were swept according to the changes in EC: DEC ratios[56]. As shown in Figure 4d, in the solvent environment with various EC: DEC ratios, $Li^+[EC_4]$ shows lowest energy of adsorbing on the graphite surface, while highest de-solvation energy. This indicates $Li^+[EC_4]$ is energetically favourable to adsorbing on the graphite edge planes and co-intercalate in to graphite lattice without de-solvation. By contrast, $Li^+[DEC_1EC_3]$ and $Li^+[DEC_2EC_2]$ has small de-solvation energy, which can easily strip off the solvated solvents before entering the graphite lattice. This indicates $Li^+[EC_4]$ is the culprit for the solvent co-intercalation, which is consistent with AFM observations in SI, Figure 19. However, a closer scrutiny of the Lowest Unoccupied Molecular Orbital (LUMO) of three solvation complexes, with and without considering the additional dipole-dipole interactions (Figure 4e), further indicating that both $Li^+[DEC_1EC_3]$ and $Li^+[DEC_2EC_2]$ has the poor anti-reduction capability compared with $Li^+[EC_4]$. One can find that the LUMO levels of three solvation complexes averagely drop by around X eV after adding the surrounding solvents to the simulation model. Moreover, as shown in Figure 4f, even the most stable $Li^+[EC_4]$ shows a decreased LUMO energy level after a higher ratio of DEC surrounding molecules are added. The higher DEC: EC ratio in the electrolyte, the more serious electrolyte decomposition could occur on the graphite electrode surface (SI, Figure 19).

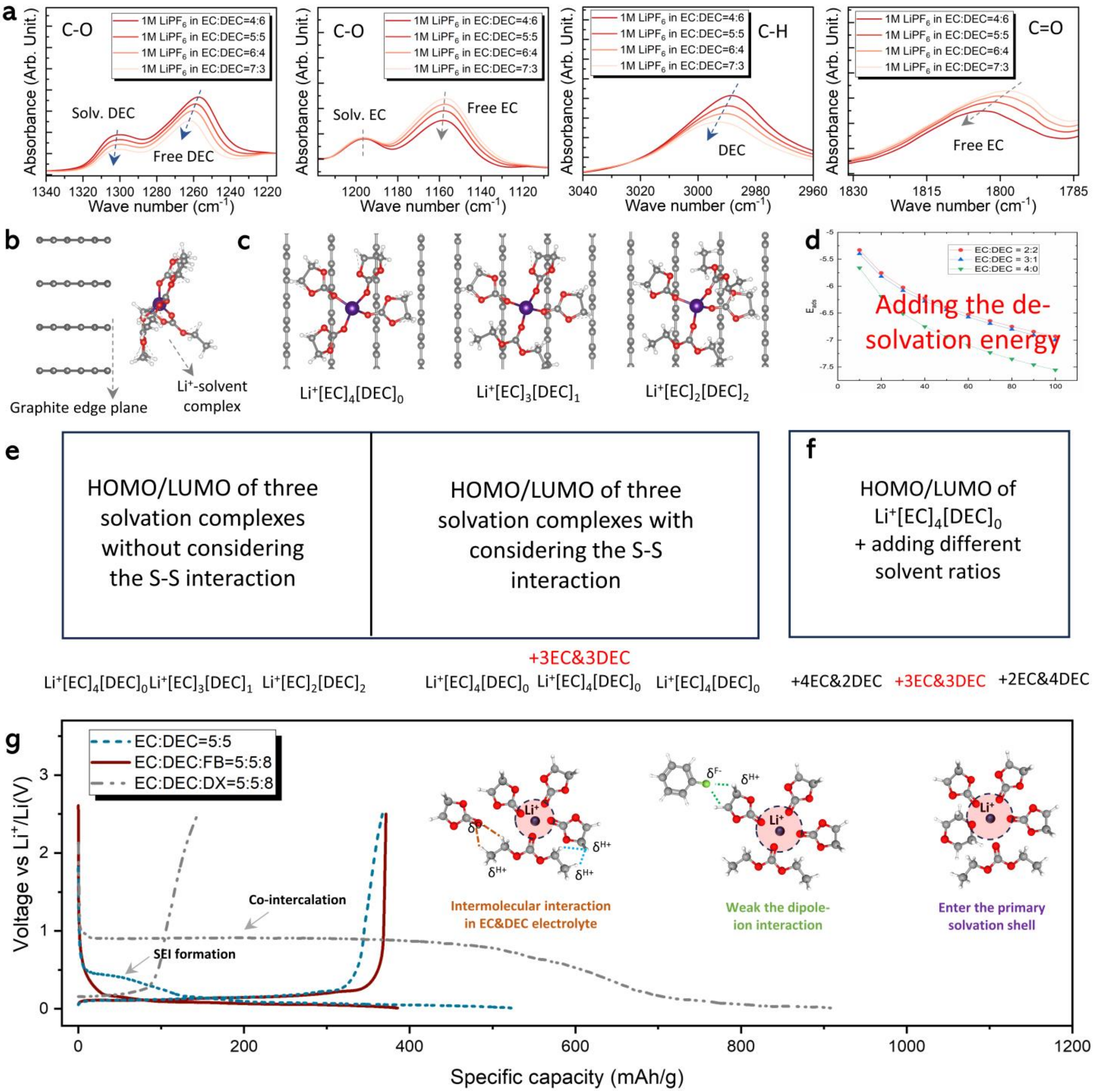

Figure 4 Effects of dipole-dipole interaction on the co-intercalation and reductive decomposition of lithium-solvent complexes. (a) FTIR spectra of 1M $LiPF_6$ electrolyte with various EC: DEC ratios. The side-view (b) and top view (c) of the structure model of three types of solvation complexes ($Li^+[EC_4]$, $Li^+[DEC_1EC_3]$ and $Li^+[DEC_2EC_2]$) adsorbing on the graphite edge planes. (d) Adsorption energy and de-solvation energy of three types of solvation complexes on the graphite edge plane. (e) The calculated HOMO and LUMO energy levels of three solvation complexes with and without adding surround solvent molecules. (f) The calculated HOMO and LUMO energy levels of $Li^+[EC_4]$ in the electrolyte with various EC:DEC ratio. (g) Formation charge-discharge curves of graphite anode in three different electrolytes. The insets are the schematic of molecular interaction of three electrolytes.

Result and discussion

Although $Li^+[EC_4]$ has the highest electrochemical stability compared with $Li^+[DEC_1EC_3]$ and $Li^+[DEC_2EC_2]$, the high de-solvation energy of $Li^+[EC_4]$ and large viscosity of the electrolyte with a high EC ratio result in serious solvent co-intercalation and a very low reversible capacity and columbic efficiency of graphite anode

(SI, Figure 20). On the other hand, $Li^+[DEC_1EC_3]$ and $Li^+[DEC_2EC_2]$ exhibit low de-solvation energy, but unsatisfied anti-reductive capability. According to the above understanding of interfacial degradation in conventional EC&DEC electrolyte, two measures can be taken: 1) reducing the cation-solvent (ion-dipole) interaction of lithium solvent complexes to enable the pure cation intercalation; and 2) optimizing the dipole-dipole interaction between the free solvents and solvated solvents to enhance the chemical stability of lithium-solvent complexes.

Adding low viscosity diluents have been used as a promising strategy to inhibit the solvent co-intercalation, as well as optimizing the solvent-solvent interaction[57-59]. Hence, as a proof of concept, non-solvating solvents, 1,4 dioxane (DX) and fluorobenzene (FB), were used as the diluents to test the ability of supressing the subsurface molecular bubble-induced interfacial degradation, as well as electrolyte reduction decompositions. The optimization experiments of the diluent concentrations are shown in SI, Figure 21. The fist galvanostatic charge/discharge curves of graphite//Li half-cell using 1 M $LiPF_6$ in EC&DEC mixing with optimized amount of FB and DX are shown in Figure 4g. We find the optimized electrolyte with FB diluent (EC: DEC: FB=5:5:8) can not only effectively supress the solvent co-intercalation, but also the SEI formation. As sketched in the inset in Figure 4g. This is probably due to moderate dipole-dipole interaction between the C-F of FB and C-H of EC molecules[52] (also see FITR in SI, Figure 22), weaking the strong coordination effect of between EC and Li^+, therefore the LUMO energy levels of lithium-EC/DEC solvation complexes are enhanced when surrounded by FB solvents (SI, Figure 23). As a result, the electrode surface stays smooth without delamination of SEI decompositions in the EC: DEC: FB=5:5:8 electrolyte. (Figure 5b). However, the graphite cycled in the electrolyte with the same amount of DX diluent shows serious solvent co-intercalation (Figure 4g) and delamination (Figure 5c). This is due to the relatively strong Li-DX coordination effect (as illustrated in the inset of Figure 4g), facilitating the DX solvent to enter the primary solvation shell (SI, Figure 24). This increases the de-solvation energy of Lithium-EC/DEC solvation complexes, resulting in the solvent co-intercalation induced graphite delamination.

Apart from the dragging effect of FB towards the solvated EC molecular, we also observed a novel interfacial molecular structure in the electrolyte with FB diluent — the preferential adsorption of FB molecules on graphite surface. As shown in Figures 5d and 5e, interfacial viscosity distributions near the graphite surface in the electrolytes with and without FB diluent are measured by AFM based force-distance spectroscopy[60,61] (SI, Figure 25). We observed the effective viscosity increases (Figure 5d) in the conventional electrolyte due to the confined effect of tip and sample surface[60,62], while a significant dropping of effective viscosity near the graphite surface was found in the electrolyte with FB diluent (Figure 5e), indicating the localized preferential adsorption and accumulation of low viscosity FB/DEC molecules on graphite surface. Since the FB diluent is less likely to enter the primary solvation shell, the low viscosity adsorption layer should mainly consist of the free uncoordinated FB solvent. This disproportion distribution of solvent near the electrode surface can greatly affect anode-electrolyte interfacial compatibility[63]. The preferential accumulation of FB on the graphite-electrolyte interface was also confirmed by DFT calculation in Figure 5f, in which we found the FB has the lowest adsorption energy on the graphite surface compared with EC DEC and DX. The preferential accumulation of electrochemically stable FB molecular layer can act as an inner molecule protection layer to prevent the solvent co-intercalation and decomposition. As a result, even less electrolyte decomposition and passivation occur on the graphite anode surface in the electrolyte with FB diluent (SI, Figure 24), the cycle stability of graphite//LCO cell using EC&DEC based electrolyte with FB diluent great exceeds that of cells without FB diluent (Figure 5g). The time and energy consuming formation process can be avoided in the optimized electrolyte with FB diluent.

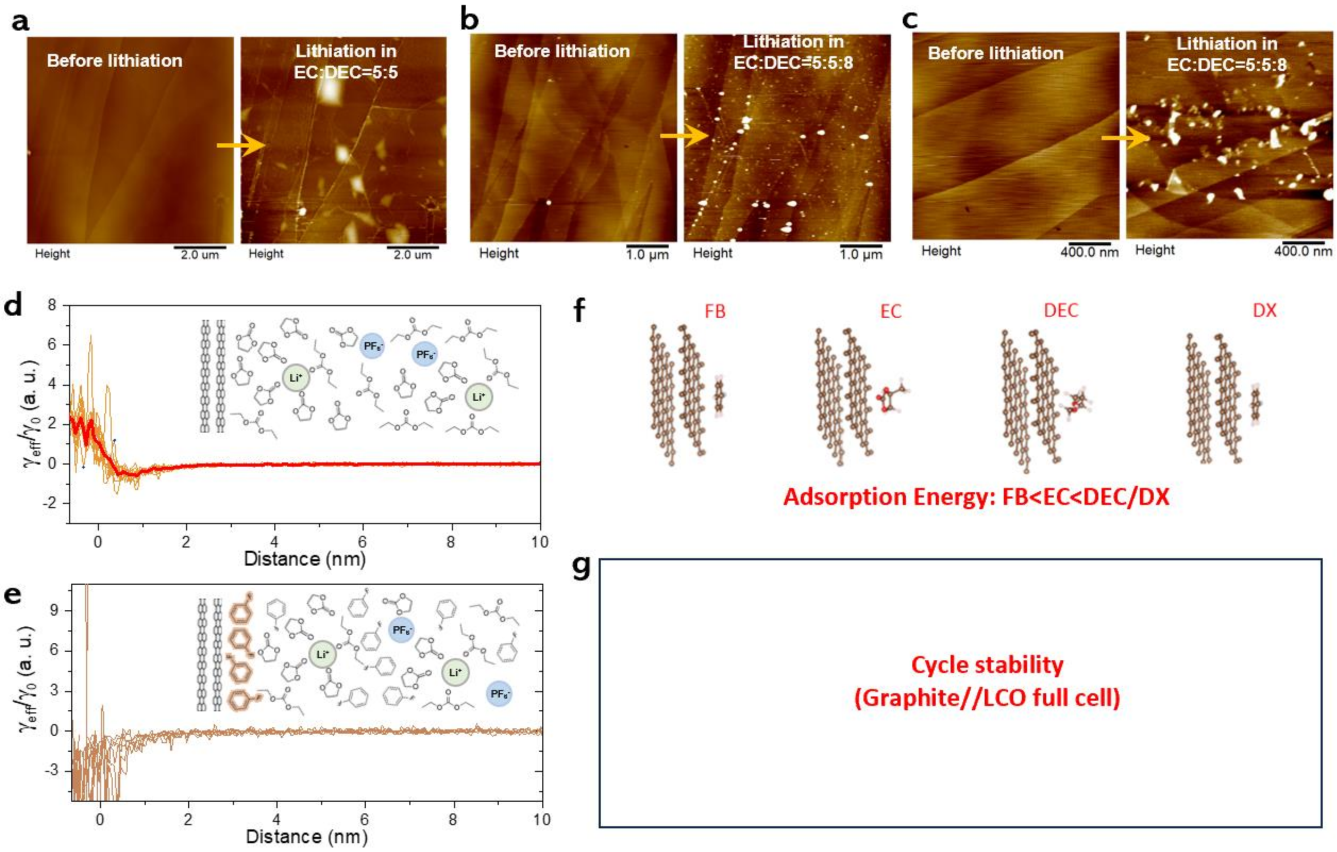

Figure 5 Interfacial molecular structure of electrolyte with and without diluent. AFM topography images of electrode surface in (a) EC: DEC=5:5, (b) EC: DEC: FB=5:5:8 and (c) EC: DEC: DX=5:5:8 electrolytes before and after the 1st lithiation. Force-distance-curves (FDC) measured on graphite anode surface in (d) EC: DEC=5:5 and (e) EC: DEC: FB=5:5:8 electrolytes. (f) Adsorption Energies of FB, EC, DEC and DX molecules on graphite surface. (g) Cycle stability LCO//Graphite full cells using commercial electrolyte and optimized EC: DEC: FB=5:5:8 electrolytes.

Conclusion

In this work, we introduced, for the first time, the ultrasonic based EC-AFM to study the nanoscale SEI formation and subsurface gas evolution of graphite anode during lithiation/de-lithiation. We observed the subsurface gas evolution starts simultaneously with solvent co-intercalation (< ~0.85 V vs Li^+/Li) during the lithiation. Interestingly, *operando* AFM characterization revealed the bubbles trapped in the carbon interlayer derive from the decomposition of co-intercalated solvents, and therefore solvent co-intercalation and decomposition at edge planes are the essential precondition for the formation of subsurface molecule bubbles XXX.

Experimental Methods

XXX

Acknowledgements

The authors wish to acknowledge the financial support from XXX the Faraday Institution (grant number FIRG018), EU Graphene Flagship Core 3 project and EPSRC project EP/V00767X/1. We are also grateful to Bruker UK, Leica Instruments, LMA Ltd. The authors also acknowledge scientific insights by NEXGENNA consortium in the new methodology development.

References

1 Wood, D. L., Li, J. & An, S. J. Formation Challenges of Lithium-Ion Battery Manufacturing. *Joule* **3**, 2884-2888, doi:10.1016/j.joule.2019.11.002 (2019).
2 Liu, T. *et al.* In situ quantification of interphasial chemistry in Li-ion battery. *Nature nanotechnology* **14**, 50-56, doi:10.1038/s41565-018-0284-y (2019).
3 Xiang, Y. *et al.* Gas induced formation of inactive Li in rechargeable lithium metal batteries. *Nature communications* **14**, 177, doi:10.1038/s41467-022-35779-0 (2023).
4 An, S. J. *et al.* The state of understanding of the lithium-ion-battery graphite solid electrolyte interphase (SEI) and its relationship to formation cycling. *Carbon* **105**, 52-76, doi:10.1016/j.carbon.2016.04.008 (2016).
5 Tu, S. *et al.* Fast-charging capability of graphite-based lithium-ion batteries enabled by Li3P-based crystalline solid–electrolyte interphase. *Nature Energy*, doi:10.1038/s41560-023-01387-5 (2023).
6 Bernhard, R., Metzger, M. & Gasteiger, H. A. Gas Evolution at Graphite Anodes Depending on Electrolyte Water Content and SEI Quality Studied by On-Line Electrochemical Mass Spectrometry. *Journal of The Electrochemical Society* **162**, A1984-A1989, doi:10.1149/2.0191510jes (2015).
7 Michalak, B. *et al.* Gas Evolution in LiNi0.5Mn1.5O4/Graphite Cells Studied In Operando by a Combination of Differential Electrochemical Mass Spectrometry, Neutron Imaging, and Pressure Measurements. *Analytical chemistry* **88**, 2877-2883, doi:10.1021/acs.analchem.5b04696 (2016).
8 Zhang, S. S. Insight into the Gassing Problem of Li-ion Battery. *Frontiers in Energy Research* **2**, doi:10.3389/fenrg.2014.00059 (2014).
9 Gao, L. T., Huang, P., Feng, J., Zhu, R. & Guo, Z. S. In Situ Characterization and Phase-Filed Modeling of the Interaction between Dendrites and Gas Bubbles during an Electrochemical Process. *ChemElectroChem* **8**, 2881-2887, doi:10.1002/celc.202100481 (2021).
10 Dreyer, S. L., Kondrakov, A., Janek, J. & Brezesinski, T. In situ analysis of gas evolution in liquid- and solid-electrolyte-based batteries with current and next-generation cathode materials. *Journal of Materials Research* **37**, 3146-3168, doi:10.1557/s43578-022-00586-2 (2022).
11 Schwenke, K. U., Solchenbach, S., Demeaux, J., Lucht, B. L. & Gasteiger, H. A. The Impact of CO2 Evolved from VC and FEC during Formation of Graphite Anodes in Lithium-Ion Batteries. *Journal of The Electrochemical Society* **166**, A2035-A2047, doi:10.1149/2.0821910jes (2019).
12 Kitz, P. G., Lacey, M. J., Novák, P. & Berg, E. J. Operando investigation of the solid electrolyte interphase mechanical and transport properties formed from vinylene carbonate and fluoroethylene carbonate. *Journal of Power Sources* **477**, doi:10.1016/j.jpowsour.2020.228567 (2020).
13 Schiele, A. *et al.* The Critical Role of Fluoroethylene Carbonate in the Gassing of Silicon Anodes for Lithium-Ion Batteries. *ACS Energy Letters* **2**, 2228-2233, doi:10.1021/acsenergylett.7b00619 (2017).
14 Han, C. *et al.* A review of gassing behavior in Li4Ti5O12-based lithium ion batteries. *Journal of Materials Chemistry A* **5**, 6368-6381, doi:10.1039/c7ta00303j (2017).
15 Zhang, L., Tsolakidou, C., Mariyappan, S., Tarascon, J.-M. & Trabesinger, S. Unraveling gas evolution in sodium batteries by online electrochemical mass spectrometry. *Energy Storage Materials* **42**, 12-21, doi:https://doi.org/10.1016/j.ensm.2021.07.005 (2021).
16 Du, W. *et al.* In-situ X-ray tomographic imaging study of gas and structural evolution in a commercial Li-ion pouch cell. *Journal of Power Sources* **520**, doi:10.1016/j.jpowsour.2021.230818 (2022).
17 Goers, D. *et al.* In situ neutron radiography of lithium-ion batteries: the gas evolution on graphite electrodes during the charging. *Journal of Power Sources* **130**, 221-226, doi:10.1016/j.jpowsour.2003.11.065 (2004).
18 Deng, Z. *et al.* Ultrasonic Scanning to Observe Wetting and “Unwetting” in Li-Ion Pouch Cells. *Joule* **4**, 2017-2029, doi:10.1016/j.joule.2020.07.014 (2020).
19 Louli, A. J. *et al.* Diagnosing and correcting anode-free cell failure via electrolyte and morphological analysis.

Nature Energy **5**, 693-702, doi:10.1038/s41560-020-0668-8 (2020).

20 Dollekamp, E., Bampoulis, P., Poelsema, B., Zandvliet, H. J. & Kooij, E. S. Electrochemically Induced Nanobubbles between Graphene and Mica. *Langmuir* **32**, 6582-6590, doi:10.1021/acs.langmuir.6b00777 (2016).

21 An, H. *et al.* Graphene Nanobubbles Produced by Water Splitting. *Nano letters* **17**, 2833-2838, doi:10.1021/acs.nanolett.6b05183 (2017).

22 Song, H.-Y. & Jeong, S.-K. Investigating continuous co-intercalation of solvated lithium ions and graphite exfoliation in propylene carbonate-based electrolyte solutions. *Journal of Power Sources* **373**, 110-118, doi:10.1016/j.jpowsour.2017.11.015 (2018).

23 Jeong, S.-K., Inaba, M., Abe, T. & Ogumi, Z. Surface Film Formation on Graphite Negative Electrode in Lithium-Ion Batteries: AFM Study in an Ethylene Carbonate-Based Solution. *Journal of The Electrochemical Society* **148**, doi:10.1149/1.1387981 (2001).

24 House, R. A. *et al.* Superstructure control of first-cycle voltage hysteresis in oxygen-redox cathodes. *Nature* **577**, 502-508, doi:10.1038/s41586-019-1854-3 (2020).

25 House, R. A. *et al.* Detection of trapped molecular O2 in a charged Li-rich cathode by Neutron PDF. *Energy & Environmental Science* **15**, 376-383, doi:10.1039/d1ee02237g (2022).

26 Shin, D. *et al.* Growth dynamics and gas transport mechanism of nanobubbles in graphene liquid cells. *Nature communications* **6**, 6068, doi:10.1038/ncomms7068 (2015).

27 Yamanaka, K., Ogiso, H. & Kolosov, O. Ultrasonic force microscopy for nanometer resolution subsurface imaging. *Applied Physics Letters* **64**, 178-180, doi:10.1063/1.111524 (1994).

28 Robinson, B. J. & Kolosov, O. V. Probing nanoscale graphene-liquid interfacial interactions via Ultrasonic Force Spectroscopy. *Nanoscale*, doi:10.1039/c4nr01348d (2014).

29 Dinelli, F., Biswas, S. K., Briggs, G. A. D. & Kolosov, O. V. Measurements of stiff-material compliance on the nanoscale using ultrasonic force microscopy. *Physical Review B* **61**, 13995-14006, doi:10.1103/PhysRevB.61.13995 (2000).

30 Huo, H. *et al.* Evaluating Interfacial Stability in Solid-State Pouch Cells via Ultrasonic Imaging. *ACS Energy Letters* **7**, 650-658, doi:10.1021/acsenergylett.1c02363 (2022).

31 Xu, W. *et al.* Ultrasonic phased array imaging of gas evolution in a lithium-ion battery. *Cell Reports Physical Science* **4**, doi:10.1016/j.xcrp.2023.101579 (2023).

32 Wasylowski, D. *et al.* Spatially resolving lithium-ion battery aging by open-hardware scanning acoustic imaging. *Journal of Power Sources* **521**, doi:10.1016/j.jpowsour.2021.230825 (2022).

33 Stock, S. *et al.* Operando Analysis of the Gassing and Swelling Behavior of Lithium-ion Pouch Cells during Formation. *Journal of The Electrochemical Society* **170**, doi:10.1149/1945-7111/acde0f (2023).

34 Zhang, N., Eldesoky, A., Dressler, R. A. & Dahn, J. R. Surprising Dependence of the Exfoliation of Graphite During Formation on Electrolyte Composition. *Journal of The Electrochemical Society* **170**, doi:10.1149/1945-7111/ace65c (2023).

35 Weng, S. *et al.* Kinetic Limits of Graphite Anode for Fast-Charging Lithium-Ion Batteries. *Nanomicro Lett* **15**, 215, doi:10.1007/s40820-023-01183-6 (2023).

36 Khestanova, E., Guinea, F., Fumagalli, L., Geim, A. K. & Grigorieva, I. V. Universal shape and pressure inside bubbles appearing in van der Waals heterostructures. *Nature communications* **7**, 12587, doi:10.1038/ncomms12587 (2016).

37 Sanchez, D. A. *et al.* Mechanics of spontaneously formed nanoblisters trapped by transferred 2D crystals. *Proc Natl Acad Sci U S A* **115**, 7884-7889, doi:10.1073/pnas.1801551115 (2018).

38 Jia, P. *et al.* Programmable graphene nanobubbles with three-fold symmetric pseudo-magnetic fields. *Nature communications* **10**, 3127, doi:10.1038/s41467-019-11038-7 (2019).

39 Ghorbanfekr-Kalashami, H., Vasu, K. S., Nair, R. R., Peeters, F. M. & Neek-Amal, M. Dependence of the shape of graphene nanobubbles on trapped substance. *Nature communications* **8**, 15844, doi:10.1038/ncomms15844 (2017).

40 Ko, H. C. *et al.* High-Resolution Characterization of Preferential Gas Adsorption at the Graphene-Water Interface. *Langmuir* **32**, 11164-11171, doi:10.1021/acs.langmuir.6b01656 (2016).

41 Cui, T. *et al.* Fatigue of graphene. *Nature materials* **19**, 405-411, doi:10.1038/s41563-019-0586-y (2020).

42 Zamborlini, G. *et al.* Nanobubbles at GPa Pressure under Graphene. *Nano letters* **15**, 6162-6169, doi:10.1021/acs.nanolett.5b02475 (2015).

43 Kumar, R. *et al.* In Situ and Operando Investigations of Failure Mechanisms of the Solid Electrolyte Interphase on Silicon Electrodes. *ACS Energy Letters* **1**, 689-697, doi:10.1021/acsenergylett.6b00284 (2016).

44 Kolosov, O. & Yamanaka, K. Nonlinear Detection of Ultrasonic Vibrations in an Atomic Force Microscope. *Jpn. J. Appl. Phys.* **32**, L1095-L1098, doi:10.1143/jjap.32.l1095 (1993).

45 Garcia, R. Nanomechanical mapping of soft materials with the atomic force microscope: methods, theory and applications. *Chemical Society Reviews* **49**, 5850-5884, doi:10.1039/d0cs00318b (2020).

46 Castellanos-Gomez, A. *et al.* Elastic Properties of Freely Suspended MoS2 Nanosheets. *Adv. Mater.* **24**, 772-+,

doi:10.1002/adma.201103965 (2012).

47 Zhang, Z. *et al.* Operando Electrochemical Atomic Force Microscopy of Solid–Electrolyte Interphase Formation on Graphite Anodes: The Evolution of SEI Morphology and Mechanical Properties. *ACS Appl. Mater. Interfaces* **12**, 35132-35141, doi:10.1021/acsami.0c11190 (2020).

48 Chen, Y. *et al.* Nanoarchitecture factors of solid electrolyte interphase formation via 3D nano-rheology microscopy and surface force-distance spectroscopy. *Nature communications* **14**, 1321, doi:10.1038/s41467-023-37033-7 (2023).

49 Huang, S., Cheong, L.-Z., Wang, S., Wang, D. & Shen, C. In-situ study of surface structure evolution of silicon anodes by electrochemical atomic force microscopy. *Appl. Surf. Sci.* **452**, 67-74, doi:10.1016/j.apsusc.2018.05.020 (2018).

50 Wang, M. *et al.* Effect of LiFSI Concentrations To Form Thickness- and Modulus-Controlled SEI Layers on Lithium Metal Anodes. *The Journal of Physical Chemistry C* **122**, 9825-9834, doi:10.1021/acs.jpcc.8b02314 (2018).

51 Sole, C., Drewett, N. E. & Hardwick, L. J. Insitu Raman study of lithium-ion intercalation into microcrystalline graphite. *Faraday Discuss.* **172**, 223-237, doi:10.1039/c4fd00079j (2014).

52 Qin, M. *et al.* Dipole–dipole interactions for inhibiting solvent co-intercalation into a graphite anode to extend the horizon of electrolyte design. *Energy & Environmental Science* **16**, 546-556, doi:10.1039/d2ee03626f (2023).

53 Wang, Y. *et al.* Weak Solvent–Solvent Interaction Enables High Stability of Battery Electrolyte. *ACS Energy Letters* **8**, 1477-1484, doi:10.1021/acsenergylett.3c00052 (2023).

54 Li, J.-T. *et al.* In situ microscope FTIR spectroscopic studies of interfacial reactions of Sn–Co alloy film anode of lithium ion battery. *Journal of Electroanalytical Chemistry* **649**, 171-176, doi:10.1016/j.jelechem.2010.03.032 (2010).

55 Xu, J. *et al.* Electrolyte design for Li-ion batteries under extreme operating conditions. *Nature* **614**, 694-700, doi:10.1038/s41586-022-05627-8 (2023).

56 Yao, N. *et al.* An Atomic Insight into the Chemical Origin and Variation of the Dielectric Constant in Liquid Electrolytes. *Angewandte Chemie International Edition* **60**, 21473-21478, doi:https://doi.org/10.1002/anie.202107657 (2021).

57 Jiang, Z. *et al.* Fluorobenzene, A Low-Density, Economical, and Bifunctional Hydrocarbon Cosolvent for Practical Lithium Metal Batteries. *Advanced Functional Materials* **31**, doi:10.1002/adfm.202005991 (2020).

58 Li, Z. *et al.* Critical Review of Fluorinated Electrolytes for High-Performance Lithium Metal Batteries. *Advanced Functional Materials* **33**, doi:10.1002/adfm.202300502 (2023).

59 Lei, S. *et al.* Nonpolar Cosolvent Driving LUMO Energy Evolution of Methyl Acetate Electrolyte to Afford Lithium-Ion Batteries Operating at −60 °C. *Advanced Functional Materials* **33**, doi:10.1002/adfm.202301028 (2023).

60 Maali, A., Cohen-Bouhacina, T., Couturier, G. & Aime, J. P. Oscillatory dissipation of a simple confined liquid. *Physical review letters* **96**, 086105, doi:10.1103/PhysRevLett.96.086105 (2006).

61 Bonaccurso, E., Kappl, M. & Butt, H. Thin liquid films studied by atomic force microscopy. *Current Opinion in Colloid & Interface Science* **13**, 107-119, doi:10.1016/j.cocis.2007.11.010 (2008).

62 Guriyanova, S., Mairanovsky, V. G. & Bonaccurso, E. Superviscosity and electroviscous effects at an electrode/aqueous electrolyte interface: an atomic force microscope study. *J Colloid Interface Sci* **360**, 800-804, doi:10.1016/j.jcis.2011.04.072 (2011).

63 Suzuki, Y. *et al.* Disproportionation Phenomenon at the Silica Interface of Propylene Carbonate–1,2-Dimethoxyethane Binary Solvent Containing Lithium Perchlorate. *The Journal of Physical Chemistry C* **126**, 11810-11821, doi:10.1021/acs.jpcc.2c02980 (2022).

Supplementary information

Subsurface molecular bubbles: the ignored interfacial degradation factor of LIBs graphite anode

Yue Chen [a, b, c 1], Wenye Xuan [d, e 1], Weijian Zhang [a, f], Nagarathinam, Mangayarkarasi [b, c], Shaohua Zhang [a, f], Jianming Tao [a, g], Jiaxin Li [a, f], Long Zhang [a], Yingbin Lin* [a, f], Yubiao Niu [h], Hsin-Yi Tiffany Chen* [e], Svetlana Menkin Bachbut [b, i], Dominic Wright [b, i], Clare P. Grey [b, i], Oleg V. Kolosov* [b, c] and Zhigao Huang* [a, g]

[a] College of Physics and Energy, Fujian Normal University, Fujian Provincial Key Laboratory of Quantum Manipulation and New Energy Materials, Fuzhou 350117, China

[b] The Faraday Institution, Quad One, Harwell Science and Innovation Campus, Didcot OX11 0RA, UK

[c] Department of Physics, Lancaster University, Lancaster LA1 4YB, UK

[d] Department of Chemistry, University of Liverpool, Liverpool L69 7ZD, UK

[e] Department of Engineering and System Science, National Tsing Hua University, Hsinchu 30013, Taiwan

[f] Fujian Provincial Engineering Technical Research Centre of Solar-Energy Conversion and Stored Energy, Fuzhou 350117, China

[g] Fujian Provincial Collaborative Innovation Centre for Advanced High-Field Superconducting Materials and Engineering, Fuzhou 350117, China

[h] We Are Nium Ltd. Research Complex at Harwell (RCaH), Rutherford Appleton Laboratory, Harwell, Didcot OX11 0FA, UK

[i] Yusuf Hamied Department of Chemistry, University of Cambridge, Lensfield Road, Cambridge CB2 1EW, UK

Corresponding authors: *yblin@fjnu.edu.cn, hsinyi.tiffany.chen@gapp.nthu.edu.tw, o.kolosov@lancaster.ac.uk, zghuang@fjnu.edu.cn

[1]Y. C. and [1]W. X. contributes equally

Figure 1 *Operando* optical images graphite anode during the 0.05 C and 0.5 C formation charging.

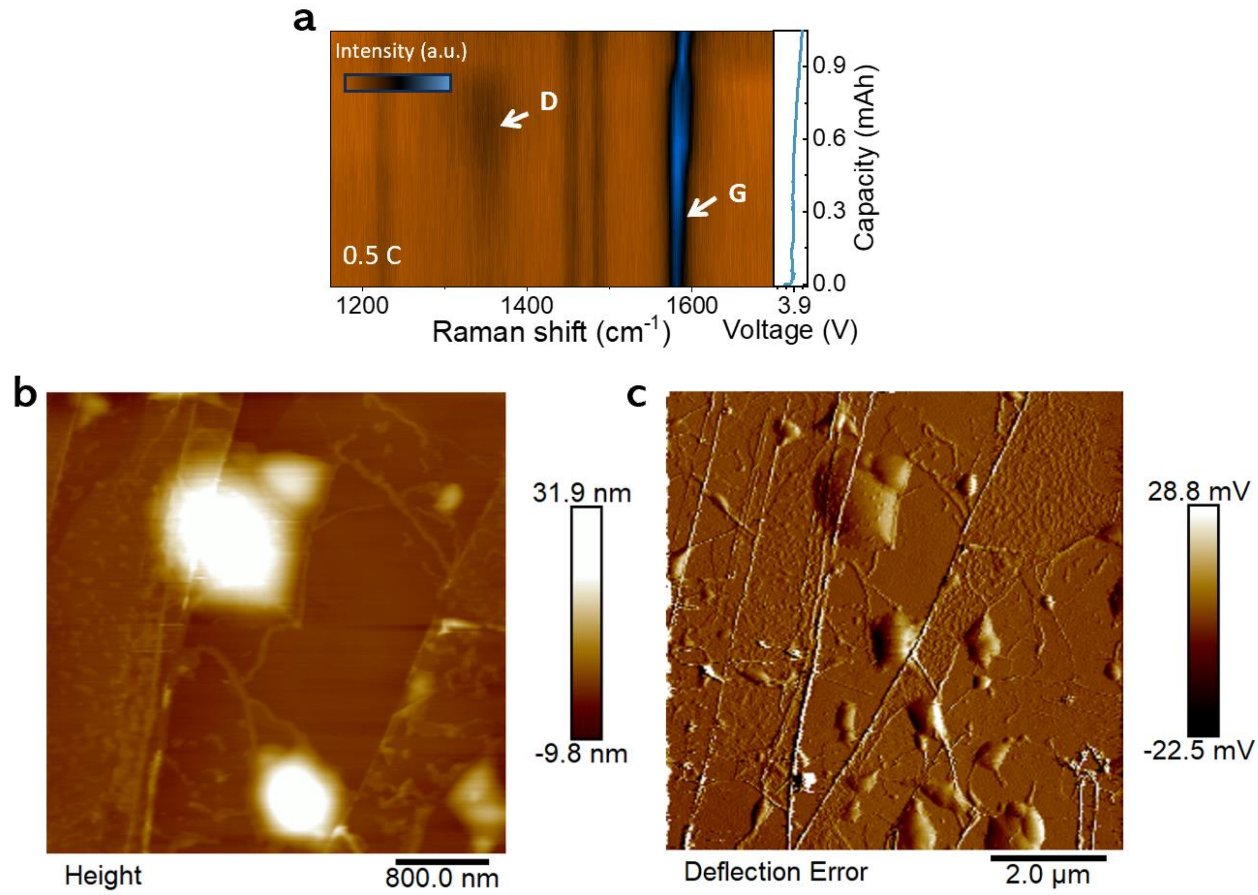

Figure 2 (a) *Operando* Raman spectroscopy of graphite anode surface lithiated in an LCO//Graphite full cell. Upon the charge, the formation of low stage number compounds causes the broadening of the G peak as it also consists of the signals from the emerging E_{2g} (at around 1575 cm^{-1})[1], but the G peak does not disappear or greatly reduced at the end of charge[2], confirming a large proportional of graphite anode was not fully lithiated into LiC_6. (b) The 4×4 μm^2 EC-AFM deflection error image of graphite surface after the 1st charge at voltage No. 4. (c) The 10×10 μm^2 EC-AFM deflection image of graphite surface after the 1st charge at voltage No. 4.

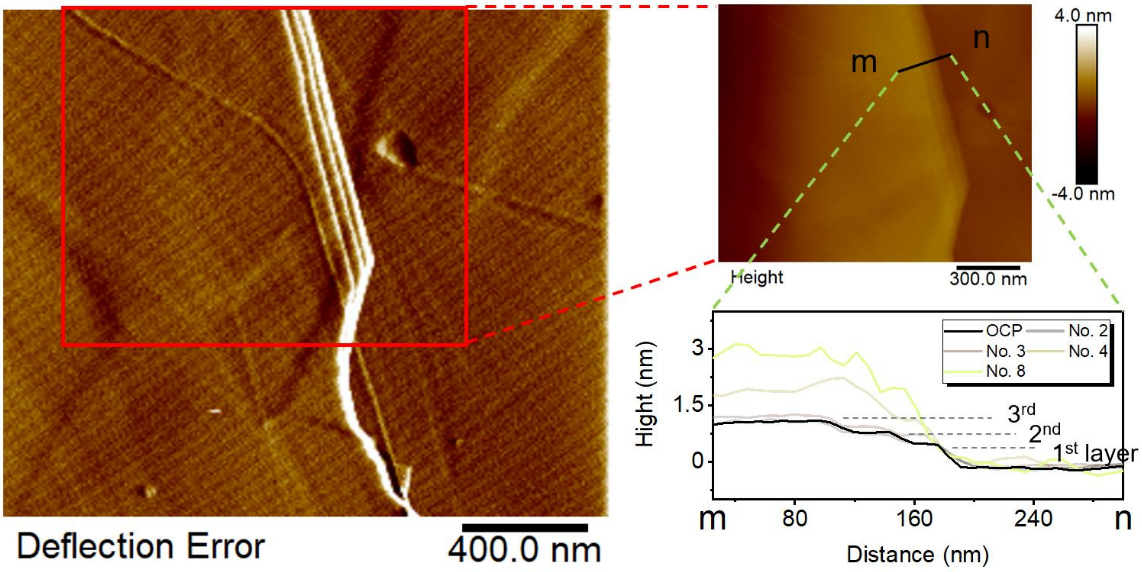

Figure 3 Structures of original carbon atomic step and the height value changes during the CV cycle.

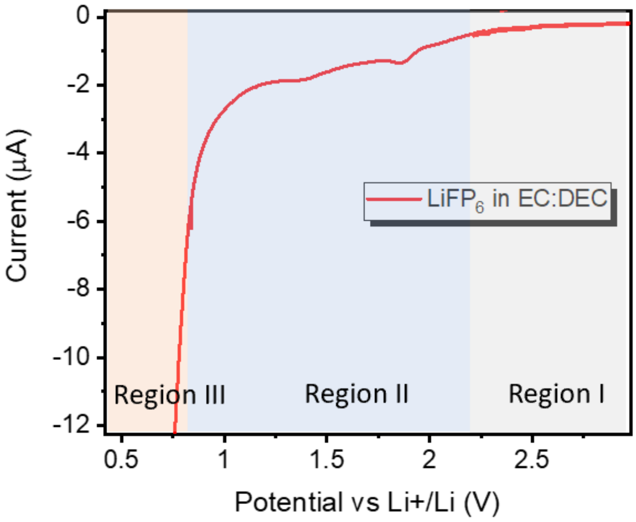

Figure 4 Enlarged CV curves during the 1st cathodic scan in main manuscript Figure 1a.

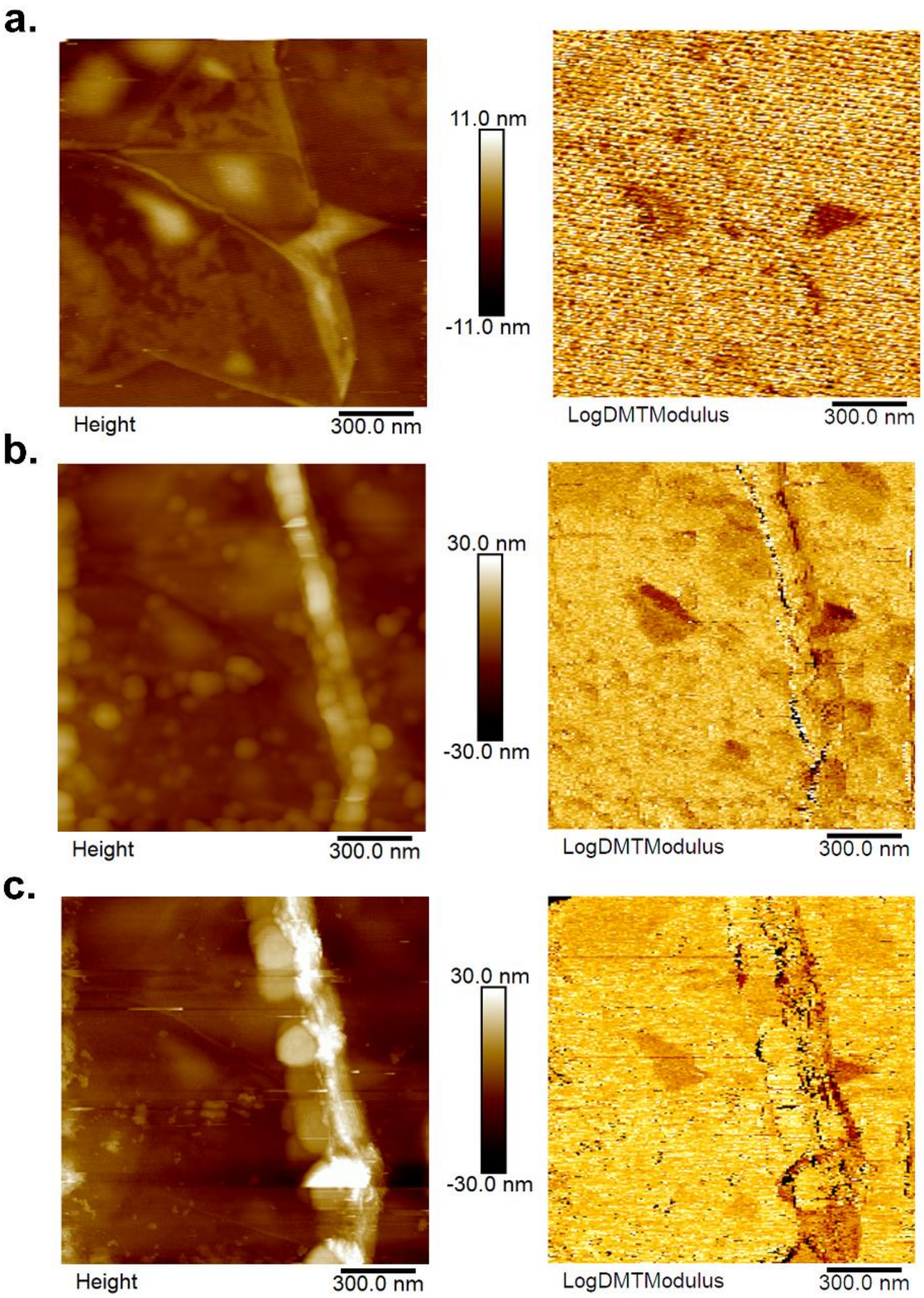

Figure 5 Surface topography and the DMT Young's modulus of the carbon atomic step after the 1st (a), 2nd (b) and 3rd (c) CV cycles measured by Peak-Force tapping mode.

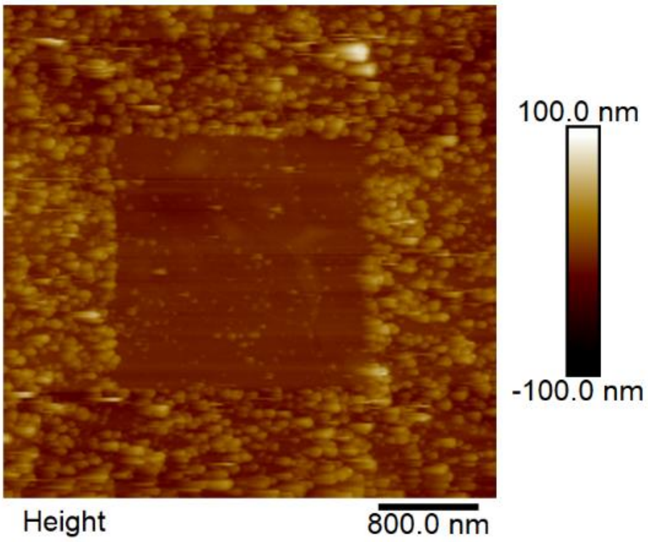

Figure 6 Electrode surface cleaned by the nano-scratching before the UFM and PeakForce tapping measurements. The remained SEI components are strongly chemically bonded on the carbon surface should be the inorganic SEI component.

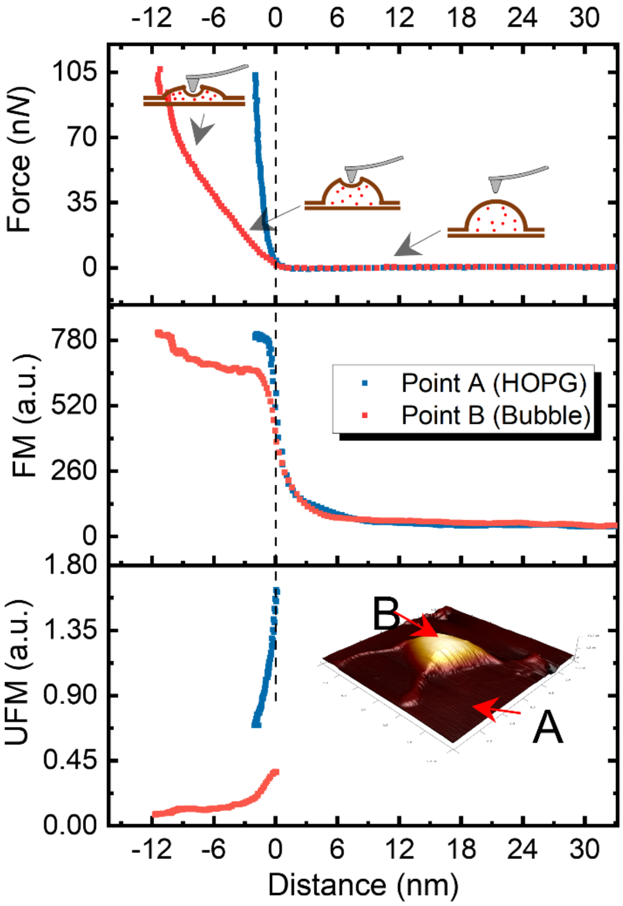

Figure 7 Force modulation and ultrasonic force modulation vs distance curves on the graphite (point A) and the bubble region (point B).

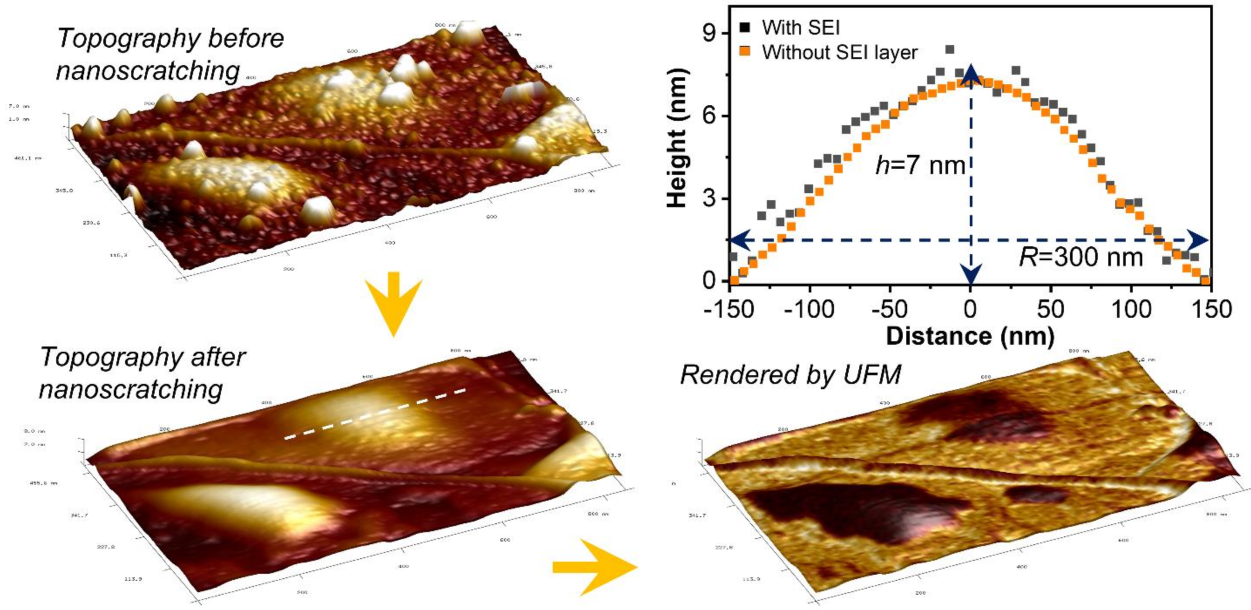

Figure 8 The nano-scratching procedure of measuring the force distance curves and the profiles of the subsurface bubble.

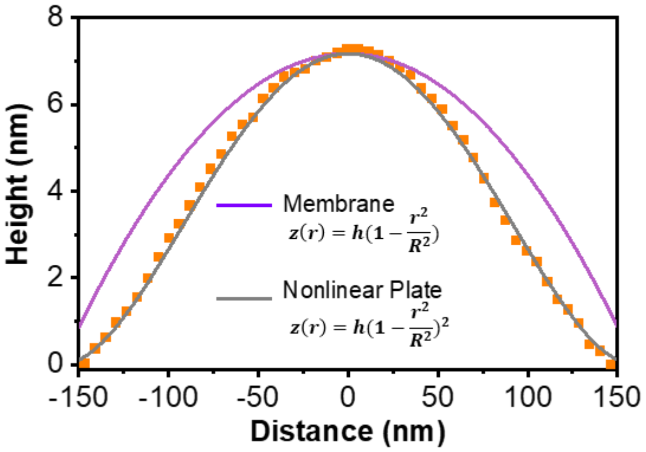

Figure 9 The profiles of a bubble in SI, Figure 8 fitting by using the Nonlinear Plate model[3,4]. The force-indentation curves can be found in supplementary note 4.

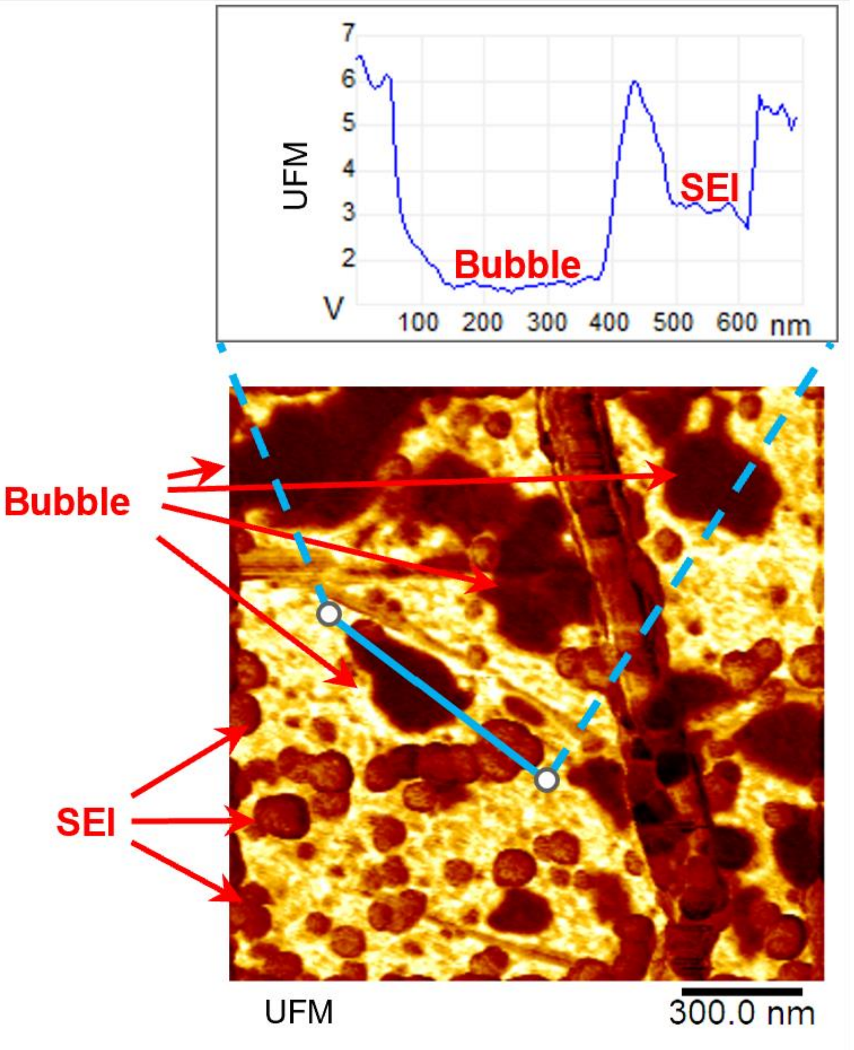

Figure 10 UFM image of electrode surface after the 2nd CV cycles

Figure 11 Fitting and simulation of the UFS curves of samples with various Young's modulus.

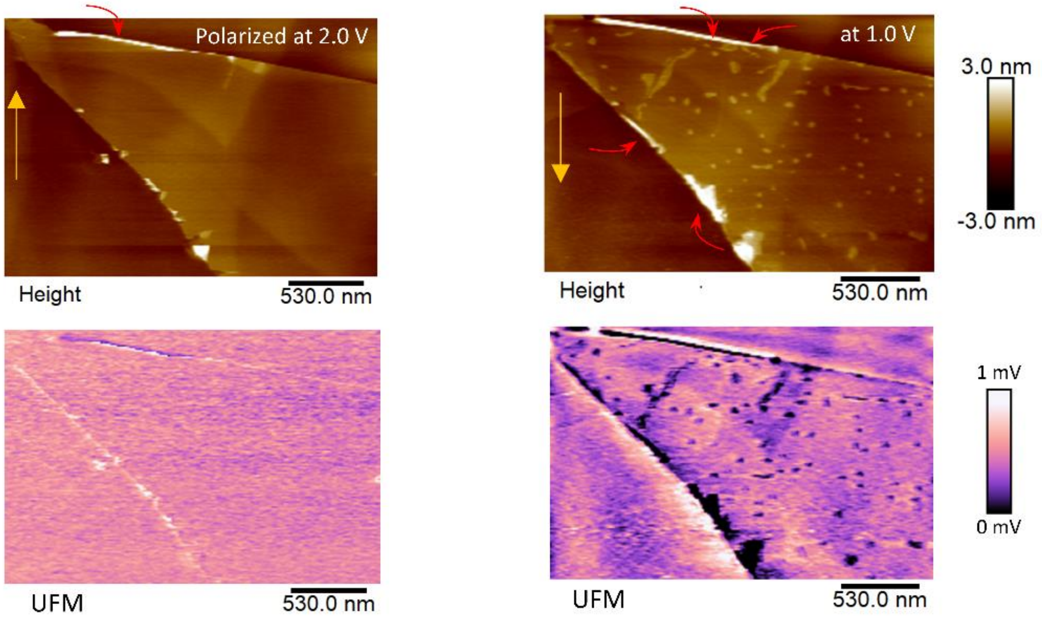

Figure 12 Surface topography and UFM images of the triple-layer graphene in Figure 3 of main manuscript under the polarization voltage of 2.0 V and 1.0 V.

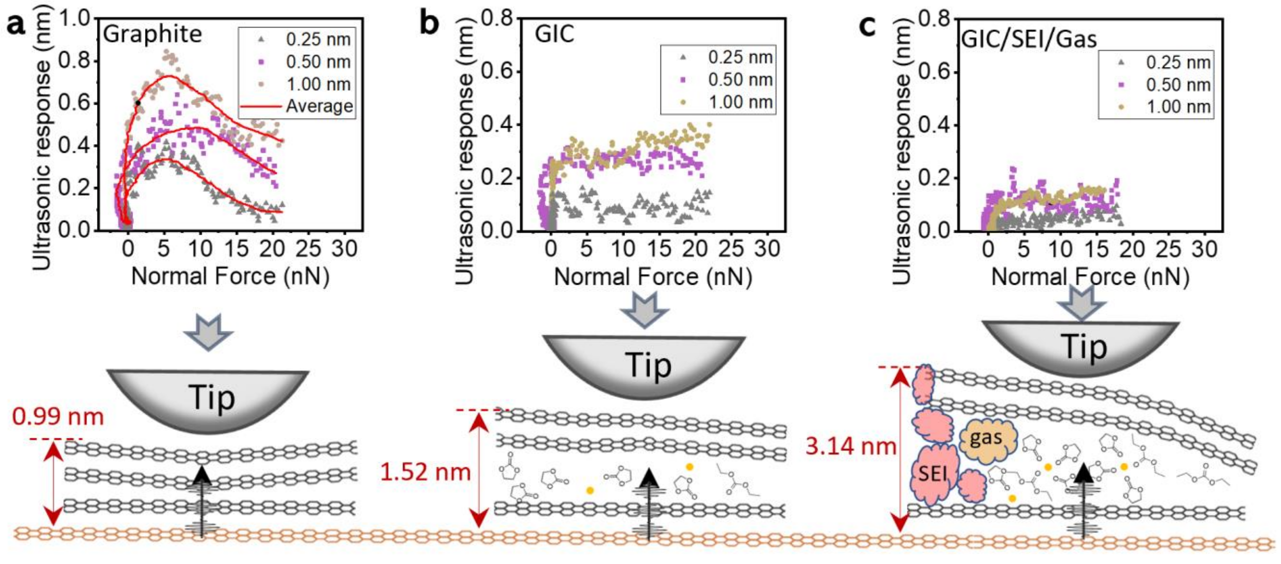

Figure 13 (a-c) The ultrasonic force spectrum (UFS) with different excitation amplitudes were recorded at the typical graphite substrate region, electrolyte-immersed region and one of the carbon step edges at the points *f*, *g* and *h*, respectively (as denoted in main manuscript, Figure 3d). On the graphite surface, the ultrasound response increases with the applied normal force until the normal force reaches about 5 n*N*, corresponding to the increased nonlinear elastic deformation of the graphite surface during the initial tip indentation. Then the ultrasound response decreases with the further increased normal force. In GIC region, the UFS shows a weaker ultrasonic response, indicating a smaller slope of the force-indentation curve (a smaller Young's modulus) compared to the graphite substrate. This region is "softer" than the original graphite due to the damping effects of the solvent molecules between carbon layers. Moreover, the UFS at carbon step edge shows negligible signal. This localised delamination region contains some soft SEI component or the initial gas products, confirming the SEI/gas accumulated at the carbon edge forms a softer and lower acoustic permittivity region compared with GIC.

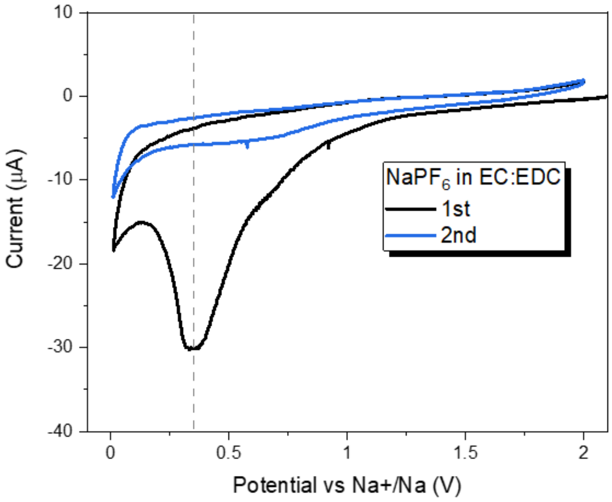

Figure 14 CV curves of TLG in $NaPF_6$ electrolyte

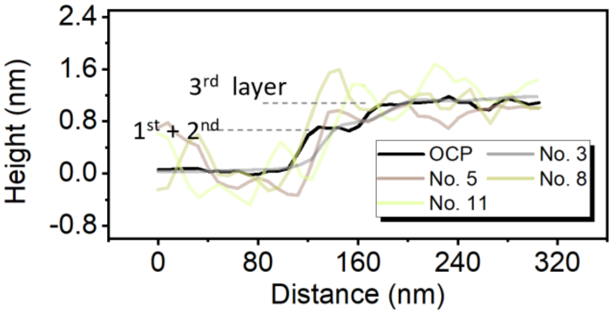

Figure 15 (a) Step height of few-layer carbon atomic steps during the sodiation.

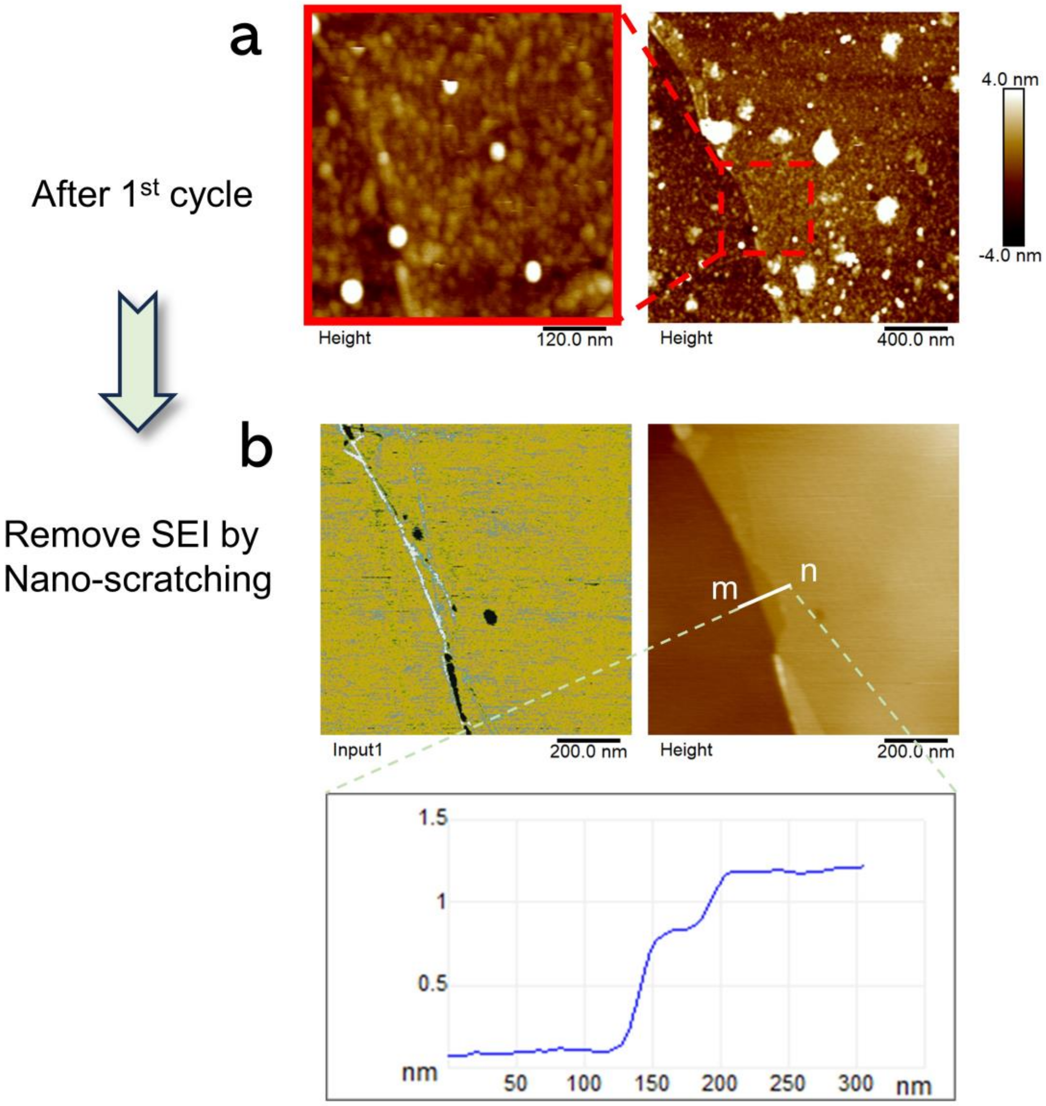

Figure 16 (a) Surface topography of TLG covered by SEI layer after the CV scan in 1M $NaPF_6$ in EC: DEC=1:1 v% electrolyte. (b) The electrode surface after nano-scratching by AFM tip. The step height is precisely measured after the nano-scratching.

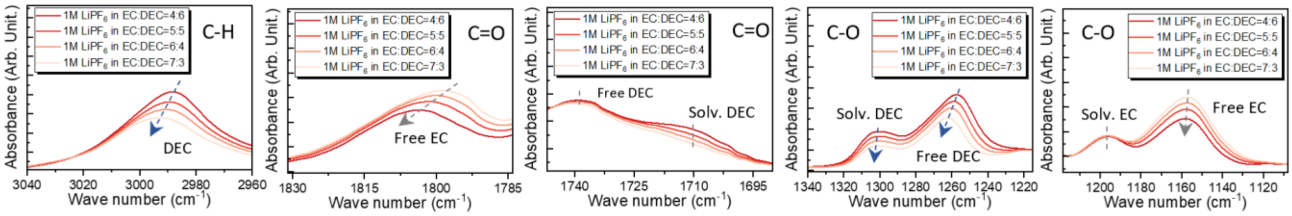

Figure 17 Full FTIR spectra of 1M $LiPF_6$ in EC & DEC electrolytes with various EC:DEC ratios.

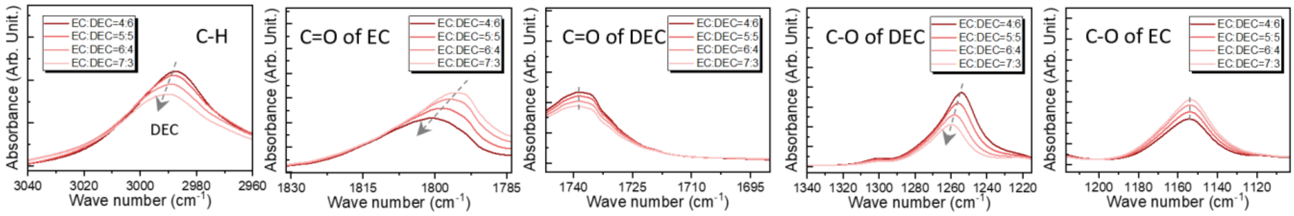

Figure 18 Full FTIR spectra of pure EC & DEC solvents with various EC:DEC ratios.

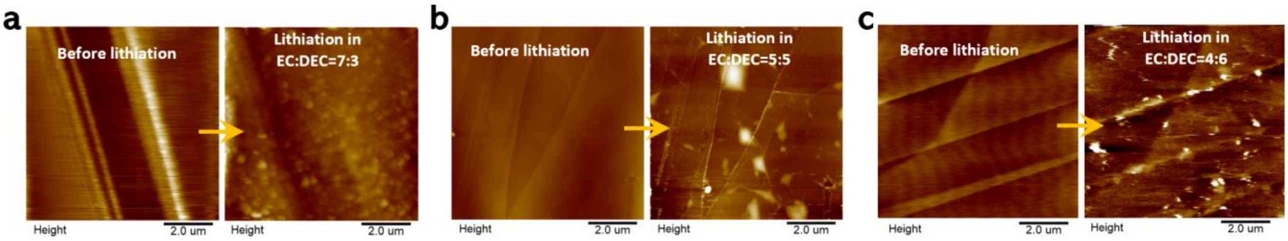

Figure 19 AFM topography images of HOPG with different EC:DEC ratios of (a) 7:3, (b) 5:5 and (c) 4:6.

Figure 20 Low initial columbic efficiency of graphite cycling in high EC: DEC ratio electrolyte.

Figure 21 The initial charge/discharge curves of the electrolytes with different ratios of FB and DX diluents

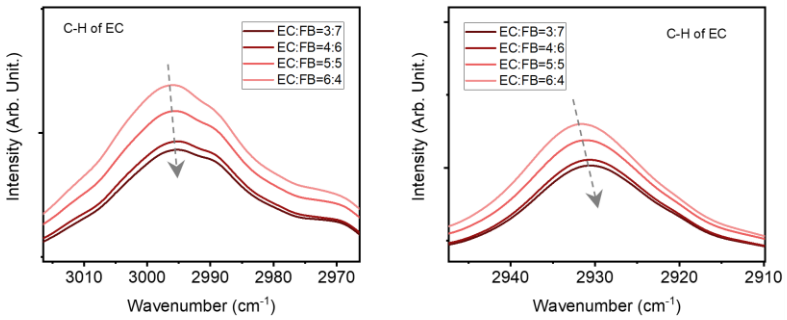

Figure 22 The red shift of C-H band of EC with the increasing of FB ratio.

Figure 23 LUMO energy levels of lithium-EC/DEC solvation complexes surrounded by FB solvents

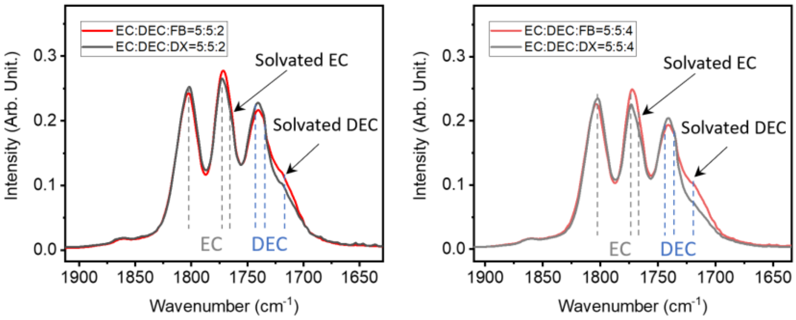

Figure 24 The C=O FTIR peaks of 1M LiPF6 in EC: DEC=1:1 electrolyte after adding 20 v% and 40 v% FB and DX diluents.

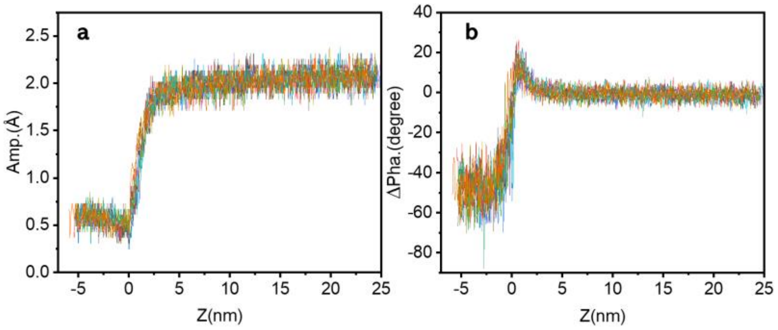

Figure 25 Ten overlapped (a) amplitude and (b) phase *vs* distance curves measured by AFM on graphite surface in 1 M LiPF6 in EC: DEC=1:1 v% electrolyte.

Supplementary Note

Supplementary Note 1 Ultrasonic Force microscopy (UFM)

1.1 Overall setups

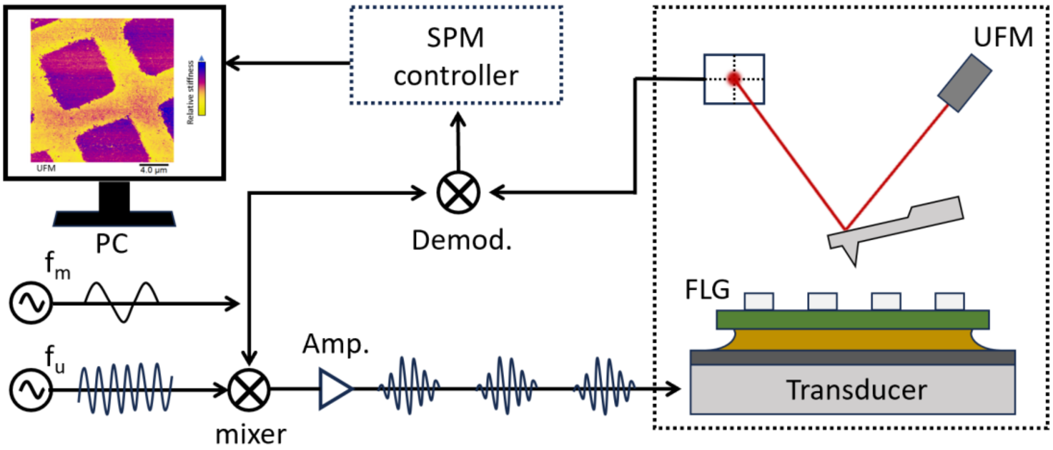

Figure 26 Schematic diagram of Ultrasonic Force microscopy (UFM)

As illustrated in Figure 26, Ultrasonic Force Microscopy (UFM) is a modification of the standard contact mode Atomic Force Microscopy (AFM). This modification involves incorporating a high frequency (HF) signal (f_u), typically ranging from 2 to 50 MHz (we utilized 2 MHz in our experiments), to induce vertical oscillation of the substrate via a dedicated piezoceramic transducer[5]. The HF oscillation is amplitude-modulated using a gated sawtooth waveform at a low kilohertz frequency (LF) (f_m). This applied oscillation generates a high-frequency displacement of the sample surface, on the order of a sub nanometre to 1-2 nanometres (to prevent damage to the Solid Electrolyte Interphase (SEI) layer). Importantly, this displacement occurs at the high frequencies well above the noncontact and contact cantilever resonances. Consequently, the AFM tip effectively remains stationary relative to the oscillation, and at the set force (indentation depth), the tip sinusoidally indents into the surface with an amplitude equal to the ultrasonic excitation amplitude. This indentation results in HF modulation of the instantaneous forces acting on the tip, and these forces can be detected due to the intrinsic nonlinearity of the tip-surface force versus distance dependence, manifesting as an additional "ultrasonic" force at the modulating low frequency[6,7].

It has been demonstrated elsewhere that the amplitude of the "ultrasonic" force consistently increases with surface stiffness (also discussed in detailed below), a characteristic applicable to a broad range of materials from polymers to rigid ceramics. This characteristic enables the effective surface mapping of nanomechanical properties with nanoscale resolution[7]. Concurrently, topography data was recorded by the stationary deflection, and nanomechanical information was captured by the average deflection of the cantilever at low modulation frequency, enabling the generation of simultaneous images depicting both topography and "nanomechanical" characteristics of few-layer graphene on the substrate.

1.2 Nonlinear detection of tip-surface interaction (ultrasonic force) and threshold ultrasonic excitation amplitude

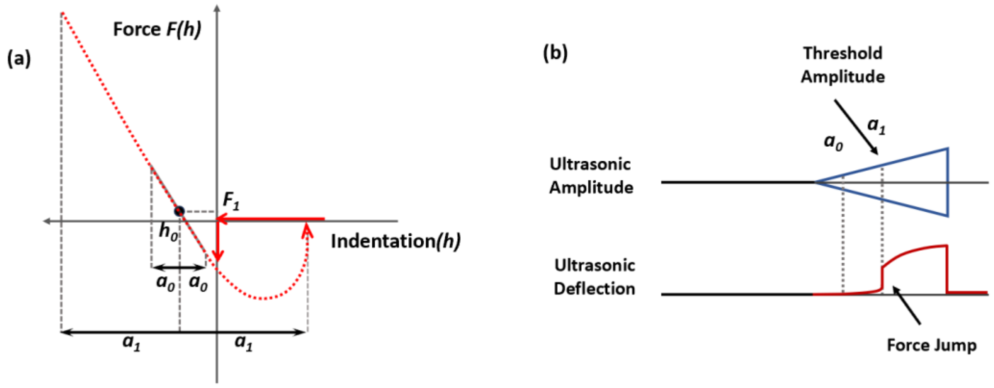

Figure 27 Schematic diagram of the (a) force-distance curve during the tip ramping to the sample surface, and (b) ultrasonic deflection (red curve) as a function of ultrasonic excitation amplitude (blue curve).

To comprehend UFM detection, let's delve into the nonlinearity of the tip-surface interaction with HF modulation during the tip indentation. In Fig. S10a, a schematic force-indentation curve is depicted. Generally, when the tip and surface are in contact, altering the direction of force, either pulling them apart or pushing them together, exhibits distinct behaviors, characterized by a pronounced "nonlinearity."

Assuming the initial normal force is set at a value F_1, modulating the indentation h_0 sinusoidally around this point yields a force averaged over one modulation cycle that is highly dependent on the modulation amplitude (a). As depicted in Figure 27a, when modulation amplitude a_0 equals h_0, no variation in the averaged normal force is anticipated. Upon reaching the pull-off point with a sufficiently high ultrasonic amplitude (a_1), contact is intermittently broken during part of the ultrasonic cycle, leading to a discontinuity in the time-averaged force. This specific ultrasonic excitation amplitude is referred to as the "threshold amplitude". It's also noteworthy that in a battery electrolyte condition, lithium/sodium ions or anions adsorption on the electrode surface screens the charges, effectively diminishing the attraction force between the tip and sample surface during approach. Consequently, the adhesion force is significantly reduced, leading to a small threshold ultrasonic excitation amplitude[8].

At the pull-off point, the corresponding normal ultrasonic deflection exhibits a noticeable jump, termed the "force jump" (see Fig. S10b). Further increments in ultrasonic amplitude result in a continuous rise in the time-averaged force and, consequently, the quasistatic normal ultrasonic deflection. The normal "*ultrasonic force*", modified by the ultrasonic vibration, can be expressed as a function F_m (h_0, a), contingent on the initial indentation h_0 and the ultrasonic amplitude a. The calculation of F_m is outlined as follows,

$$F_m(h_0,a)=\frac{1}{T_{ult}}\int_0^{T_{ult}}F(h_0+acos2\pi f_{ult})\,dt \qquad (1)$$

where $F(h)$ is the force dependence on the indentation depth without ultrasonic vibration, f_{ult} is the ultrasonic frequency, the integral is taken over a period $T_{ult}=1/f_{ult}$. When F_m increases due to the nonlinearity, the cantilever deflection at LF modulation frequency increases as well until a new equilibrium position is reached. This new stationary normal deflection is given by,

$$F_m(h_{eq},a)=k_{lever}d_{equ} \qquad (2)$$

where d_{equ} and h_{eq} are the new ultrasonic-induced cantilever deflection and sample indentation depth, respectively. The k_{lever} is the stational cantilever force constant considering the LF modulation frequency is below the cantilever free resonance frequency.

1.3 Effects of setpoint force, ultrasonic excitation amplitude, and modulation frequency on the ultrasonic deflection signal

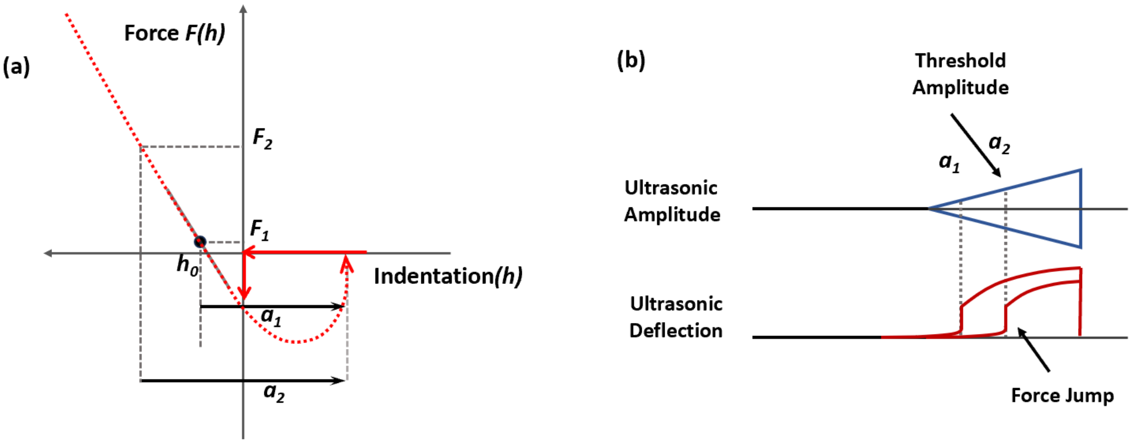

Figure 28 Schematic diagram of ultrasonic force detection under different excitation amplitude. (a) Force-indentation curves. (b) ultrasonic deflection (red curve) as a function of ultrasonic excitation amplitude (blue curve).

Both the setpoint force, ultrasonic excitation amplitude, and LF modulation frequency have great impacts on the detection of the ultrasonic deflection signal. As shown in Figure 28, the threshold amplitude is observed to be dependent on the set normal force value. The higher setpoint force requires a larger ultrasonic excitation amplitude to reach the pull-off point, such that the threshold amplitude $a(F_2) = a_2$ is expected to be higher than the threshold amplitude $a(F_1) = a_1$. In practical experiments, an active feedback circuit is employed to correct the normal deflection and maintain the initially set value. Consequently, the key is to detect variations in normal deflection caused by the "ultrasonic force" acting on the tip. This detection is achievable by modulating the amplitude of ultrasonic vibration at a frequency higher than the feedback cutoff frequency of AFM circuit, preventing the feedback from correcting normal deflection variations. For our commercial system, the cutoff frequency is approximately 1 kHz for commonly used loop-gain values. However, this cutoff value can be further reduced by decreasing the loop gain, a choice heavily reliant on the scan speed.

Supplementary note 2 Effective Young’s modulus studied by Ultrasonic force spectroscopy (UFS)

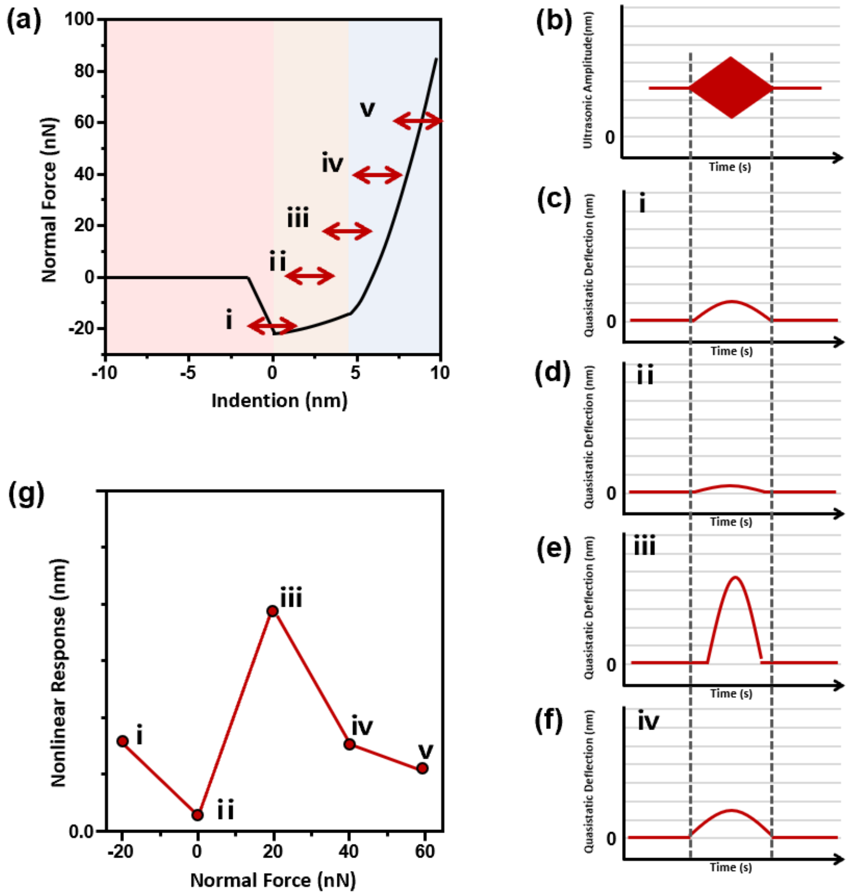

Figure 29 (a-f) Schematics of UFS detections during the force-distance curve measurement at preset forces i, ii, iii and iv, and (b) The obtained UFS curve.

As shown in Figures 29a-f, by conducting force-distance curves and concurrently recording UFM response at various preset force values, it becomes feasible to directly quantify the values of tip-surface contact stiffness. This information enables the assessment of surface elastic properties, assuming a suitable solid-solid contact model. The schematic Ultrasonic Force Spectroscopy (UFS) curves (ultrasonic deflection as a function of the normal load within the 0–60 n*N* range) are shown in Figure 30g. The detailed contact mechanisms are analysed below:

In UFS measurements, the sample undergoes harmonic oscillation at a HF, surpassing the free cantilever and contact resonances. The extreme dynamical rigidity of the cantilever ensures that the sample's vibration is not transferred to the cantilever. Consequently, it is safe to assume that the tip-surface distance oscillates at the same ultrasonic frequency (f_{ult}) with an amplitude (a). The highly nonlinear dependence of the interaction force on the tip-surface distance causes this oscillation to be "rectified," generating an additional "ultrasonic" force (F_{m}) as detailed in equation (1). The initial cantilever deflection (d_0) is defined by the set force ($F_0 = k_{\mathrm{lever}} d_0$), where k_{lever} is the cantilever spring constant. However, the presence of the additional ultrasonic force results in an extra cantilever deflection (d_{ult}), establishing a new equilibrium position for the cantilever.

$Z_{\mathrm{equ}} = d_0 + d_{\mathrm{ult}}$. (3)

In order to effectively detect d_{ult}, which depends on the effective Young’s modulus of the specimen and probe, the HF ultrasonic vibration is modulated using a gated saw-tooth signal at LF (Fig. S12b). The resulting LF cantilever vibrations are detected with high resolution by a lock-in amplifier, yielding RMS amplitude that is recorded ultrasonic deflection d_{ult}. Fig. S12g shows schematically the acquisition of the nonlinear response d_{ult} for a typical force *vs* indentation relation (Fig. S12a) with ultrasonic amplitude of a = 1 nm.

At static equilibrium, in order to sustain the pressure exerted by the tip, the surface deforms by h_{cont} that depends on the contact stiffness k_{cont}, defined as,

$$h_{cont} = \frac{\mathrm{F}_N + \mathrm{F}_C}{k_{cont}} \quad (4)$$

The equations describing it are those of a simplified 'two-spring model', valid at frequencies below the first cantilever resonance,

$$F_N + F_C = k_{lever} \times d_{lever} = k_{cont} \times h_{cont} \qquad (5)$$

However, in UFM, the excitation frequency is much higher than the first cantilever resonance (in contact with the sample) and should not coincide with any of the higher resonant modes. Working in this 'inertial' regime, the cantilever cannot follow the vertical modulation as the effective cantilever spring constant (k_{lever}^{eff}) significantly exceeds the contact stiffness,

$$k_{lever}^{eff} > k_{cont} \approx k_{lever} \times \left(\frac{f_{UFM}}{f_{Res}}\right)^{\frac{3}{2}} \gg k_{lever} \qquad (6)$$

where f_{ult} is the ultrasonic frequency and f_{Res} the first free resonant frequency of the cantilever. Since we modulate the ultrasonic amplitude at low frequency, below the cantilever resonances and above the feedback cut-off, the ultrasonic deflection d_{ult} can be detected as a quasi-static force, so that the equation (5) remains fully valid.[9]

Assuming the tip-surface contact can be describe by the Derjagin–Muller– Toropov (DMT) mode,[10]

$$r = \left[\frac{3R(F_N + F_C)}{4E^*}\right]^{1/3} \qquad (7)$$

$$r^2 = Rh_{cont} \qquad (8)$$

$$F_N + F_C = \frac{4}{3}E^* R^{1/2} h_{cont}^{3/2} \qquad (9)$$

$$F_C = 2\Delta\gamma\pi R \quad (10)$$

where r is the contact radius, $\Delta\gamma$ and F_{C} respectively the work of adhesion and the adhesion force, E^* the reduced Young's modulus, and R the tip radius.

The effective Young's modulus of tip-sample contact is,

$$\frac{1}{E^*} = \frac{(1 - v_{sample}^2)}{E_{sample}} + \frac{(1 - v_{tip}^2)}{E_{tip}} \qquad (11)$$

where E_{sample} and E_{tip} are the Young's modulus of sample surface and tip, respectively, and the v_{sample} and v_{tip} are their Poisson's ratio. The ultrasonic force can be described as,

$$F_m(h,a) = \frac{1}{T}\int_0^{T_{ult}} \left[\frac{4}{3}\frac{E_{sample}E_{tip}}{E_{tip}\left(1 - v_{sample}^2\right) + E_{sample}(1 - v_{tip}^2)} R^{\frac{1}{2}} (h + acos2\pi f_{ult})^{\frac{3}{2}} - 2\Delta\gamma\pi R\right] dt \qquad (12)$$

Therefore, ultrasonic deflection can be described as,

$$d_{lever} = \frac{F_m(h,a)}{k_{lever}} \qquad (13)$$

In each UFS measurement, f_{ult} maintains at 2 MHz, a is kept as a constant value, the indentation h is varied upon the tip indentation. Meanwhile, the PeakForce-QNM data indicate that, over sample surface, the adhesion can be considered homogeneous. Thus, the integral of $2\Delta\gamma\pi R$ term in equation (12) can be treated as a constant value. Therefore, the ultrasonic deflection is not affected by the local variations of the adhesive force. Therefore, the E_{sample} can be studied by UFS in the contact region.

Supplementary Note 3 Adhesion energy and aspect ratio of bubbles/blisters

Trapped substances sandwiched between a two-dimensional (2D) crystal, such as graphene and MoS_2[11,12], and an atomically flat substrate result in the creation of bubbles/blisters. The size, configuration, and internal pressure of these bubbles are dictated by the interplay between the van der Waals (vdW) attraction of the crystal to the substrate and the elastic energy required for deformation. This phenomenon allows for the exploration of the elastic properties of 2D crystals and the conditions of confinement through the study of bubbles/blisters.

The edges adapt to the competition between the vdW attraction and the internal pressure, while the pressure itself is determined by the adhesion between the graphene the graphite substrate, the bubble/blister profiles are found self-consistently. The vdW energy associated with separating of a graphene layer from the substrate is given by

$$E_{vdW} = \pi\gamma R^2 = \pi(\gamma_1 - \gamma_2 - \gamma_3)R^2 \qquad (14)$$

where γ_1, γ_2 and γ_3 are the adhesion energies between top graphene layers and the graphite substrate, graphene and the substance inside the nano-hills, and the substrate and the graphite substrate, respectively.

The nano-hill's height profile and volume are described respectively by

$$Z(r) = h_{max}(1 - \frac{r^2}{R^2})^2 \quad (15)$$

$$V(r) = c_V(1 - \frac{r^2}{R^2})^2 h_{max}R^2 \qquad (16)$$

Where h_{max} and R is the maximum height and effective radius of nano-hills.

The in-plane displacements and the total elastic energy $E_{elastic}$ as a function of $Z(r)$ are given

$$E_{elastic} = c_1 Z(r) Y \frac{h_{max}^3}{R^2} + c_2 Z(r) Y \epsilon h_{max}^2 \qquad (17)$$

Where c_1 is a dimensionless coefficient, Y is the 2D Young's modulus of the few-layer graphene, and R and ϵ are the effective radius and external strain of nano-hills. In the situation without external strain applied on nano-hills, $\epsilon = 0$, total elastic energy is

$$E_{elastic} = c_1(R^2 - r^2)^2 Y \frac{h_{max}^4}{R^4} \quad (18)$$

The free energy, $E_b(V)$, of substance inside the nano-hills is a function of the volume of the nano-hills. If the bubble is filled with a substance having finite compressibility, the pressure of the substance inside the nano-hills can be written as

$$P = -\frac{\partial E_b}{\partial V} \qquad (19)$$

Neglecting the bending rigidity, the total energy can be written as

$$E_{tot} = E_{vdw} + E_{elastic} + E_b(V) = = \pi(\gamma_1 - \gamma_2 - \gamma_3)R^2 + c_1(R^2 - r^2)^2 Y \frac{h_{max}^4}{R^4} + E_b(V) \, (20)$$

By minimizing the total energy with respect to h_{max} and R, and replacing P using equation (19), we obtain

$$\frac{h_{max}}{R} = (\frac{\pi\gamma}{5c_1 Y})^{1/4} \qquad (21)$$

For few-layer graphene, the coefficients $c_1 \approx 0.7$[13], 2D Young's modulus is about 340 N/m[14], therefore, the interfacial energy γ can be determined by measuring the aspect ratio of the bubble $\frac{h_{max}}{R}$.

Supplementary note 4 Force-indentation curves and layer of graphene

In the elastic plate theory, the edge of the bubble is clamped with zero slope due to a finite bending stiffness. In the membrane model, the boundary condition at the edge is relaxed, resulting in a kink (infinite curvature) at the edge. According the profile of a graphene bubble in Figure 9, our graphene bubble can be treated as a plate with certain bending rigidity. In a simplified continuum mechanics model of the plate, the relationship between the applied force at the centre of the plate and the resulting deformation is[15]

$$F = \left[\frac{4\pi E}{3(1-v^2)} \cdot \left(\frac{t^3}{R^2}\right)\right] \delta + (\pi T)\delta + (\frac{q^3 E t}{R^2})\delta^3 \qquad (22)$$

Where v and E are the Poisson ratio (0.18) and Young's modulus (1 TPa)[14,16], t is the thickness of the few-layer graphene, R is the effective radius, T is the pretention (1.25 N/m) derives from the internal pressure, and $q \approx 0.982$ is a dimensionless parameter related to the v. The first term in Equation (22) corresponds to the mechanical behaviour of a plate with certain bending rigidity. The second term represents the mechanical behaviour of a starched plate. The third term takes into account the stiffening of the layer during the force cycle which makes $F(\delta)$ nonlinear. Here, the effect of shearing stresses, on planes parallel to the surface of the plate, can be neglected because of the low plate thickness to plate radius ratio. The fitting dot plots of force-indentation curves in Figure 2j in the main manuscript were done by varying the thickness of the graphene layer at 0.142, 0.336, 0.672 and 1.008 nm to represent the bubble with 1-4 layers of graphene.

Supplementary note 5 Dynamic force-distance curves using magnetic excitation

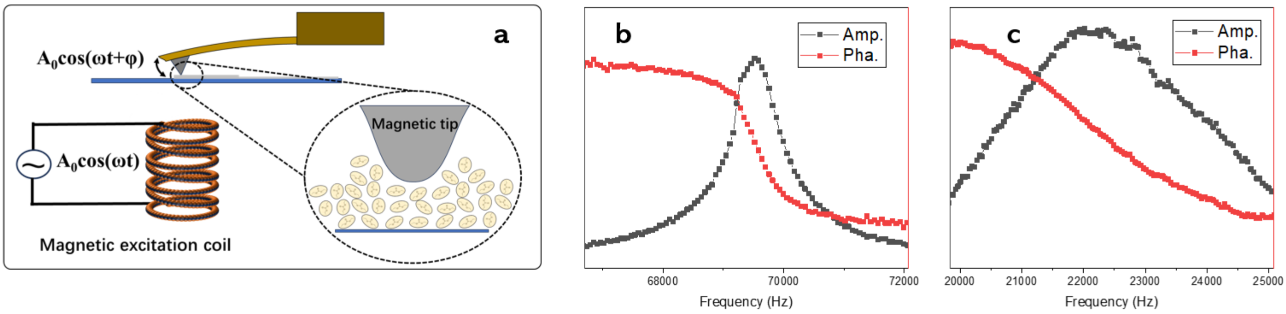

Figure 30 (a) Schematic representation of the magnetic excitation force distance measurements. The cantilever was driven at fixed tapping amplitude, and we measured simultaneously the phase and the amplitude of the cantilever as the tip approaches the graphite anode surface in liquid electrolyte. (b) The tapping amplitude and phase response near the resonance in (b) air and (c) liquid electrolyte.

The dynamic tapping force-distance curves were performed in the magnetic excitation mode as shown in Figure 30a. In our set-up, a magnetic excitation coil was placed underneath the AFM EC-cell, and drive by an oscilloscope using a sinusoidal voltage V_0=A$_0$cos(wt+φ). The cantilever, with only the tip coated by magnetic materials, can localized the driving force and oscillate at resonance frequency with a very small peak-to-peak amplitude, close to the diameter of solvent molecules. The oscillation amplitude monitored by a lock-in amplifier was maintained at around 0.2 nm in our experiments. This is roughly the half size of the solvent molecule. As shown in Figures 30b and 30c, using this localized magnetic driving can avoid the “forest of resonance peaks”, one can observe a clean resonance peak (at ~22.4 kHz) at amplitude *vs* frequency curve in liquid electrolyte using a 69 kHz cantilever (in Air). One should note that further increasing the Q factor of cantilever can even increase the sensitivity of this magnetic excited dynamic force-distance curves.

For a cantilever oscillating with a small amplitude compared to the range of the interaction length. The force induced by the confined fluid has two contributions: 1) a conservative term ($-k_{int}z$), and 2) a dissipative term ($-\gamma_{int}z$), where k_{int} and γ_{int} are the effective interaction stiffness and damping coefficient of the confined liquid, respectively, and Z is the instantaneous position of the cantilever. The motion of the cantilever is then described by[17,18]

$$m^*\ddot{z} + (\gamma_0 + \gamma_{int})\dot{z} + (k_0 + k_{int})z = F_0 e^{jwt} \quad (23)$$

Where the driving force $F_0 = k_0A_0/Q$, m* is the effective mass of the cantilever and γ_0 is the viscous hydrodynamic damping far from the surface and is related to the quality factor Q and the resonance frequency f_0 via the equation $Q= m^*w_0/\gamma_0$. k_0 is the cantilever stiffness and A$_0$ is the amplitude of the oscillation far away from the interaction region. The stationary solution $z = Ae^{j(wt+\varphi)}$ of the above equation gives the damping coefficient[18]

$$\frac{\gamma_{int}}{\gamma_0} = -\left(\frac{w_0A_0}{wA}\sin(\varphi) + 1\right) \qquad (24)$$

For each cantilever-tip-surface distance, the confined liquid can be described by a fluid having an effective viscosity proportional to the damping coefficient[19], $\mu_{eff} \propto \gamma_{int}$, therefore we interfacial viscosity can be measured through reconstructing the tapping amplitude & phase vs distance curves.

References

1 Migge, S., Sandmann, G., Rahner, D., Dietz, H. & Plieth, W. Studying lithium intercalation into graphite particles via in situ Raman spectroscopy and confocal microscopy. *Journal of Solid State Electrochemistry* **9**, 132-137, doi:10.1007/s10008-004-0563-4 (2004).

2 Neale, A. R., Milan, D. C., Braga, F., Sazanovich, I. V. & Hardwick, L. J. Lithium Insertion into Graphitic Carbon Observed via Operando Kerr-Gated Raman Spectroscopy Enables High State of Charge Diagnostics. *ACS Energy Lett* **7**, 2611-2618, doi:10.1021/acsenergylett.2c01120 (2022).

3 Khestanova, E., Guinea, F., Fumagalli, L., Geim, A. K. & Grigorieva, I. V. Universal shape and pressure inside bubbles appearing in van der Waals heterostructures. *Nature communications* **7**, 12587, doi:10.1038/ncomms12587 (2016).

4 Yue, K., Gao, W., Huang, R. & Liechti, K. M. Analytical methods for the mechanics of graphene bubbles. *Journal of Applied Physics* **112**, doi:10.1063/1.4759146 (2012).

5 Cuberes, M. T., Briggs, G. A. D. & Kolosov, O. Nonlinear detection of ultrasonic vibration of AFM cantilevers in and out of contact with the sample. *Nanotechnology* **12**, 53-59 (2001).

6 Dinelli, F., Biswas, S. K., Briggs, G. A. D. & Kolosov, O. V. Measurements of stiff-material compliance on the nanoscale using ultrasonic force microscopy. *Physical Review B* **61**, 13995-14006, doi:10.1103/PhysRevB.61.13995 (2000).

7 Bosse, J. L., Tovee, P. D., Huey, B. D. & Kolosov, O. V. Physical mechanisms of megahertz vibrations and nonlinear detection in ultrasonic force and related microscopies. *Journal of Applied Physics* **115**, 144304, doi:doi:http://dx.doi.org/10.1063/1.4871077 (2014).

8 Robinson, B. J. & Kolosov, O. V. Probing nanoscale graphene-liquid interfacial interactions via Ultrasonic Force Spectroscopy. *Nanoscale*, doi:10.1039/c4nr01348d (2014).

9 Dinelli, F., Pingue, P., Kay, N. D. & Kolosov, O. V. Subsurface imaging of two-dimensional materials at the nanoscale. *Nanotechnology* **28**, 085706, doi:10.1088/1361-6528/aa55e2 (2017).

10 Derjaguin, B. V., Muller, V. M. & Toporov, Y. P. Effect of contact deformations on the adhesion of particles. *Journal of Colloid and Interface Science* **53**, 314-326, doi:https://doi.org/10.1016/0021-9797(75)90018-1 (1975).

11 Sanchez, D. A. *et al.* Mechanics of spontaneously formed nanoblisters trapped by transferred 2D crystals. *Proc Natl Acad Sci U S A* **115**, 7884-7889, doi:10.1073/pnas.1801551115 (2018).

12 Jia, P. *et al.* Programmable graphene nanobubbles with three-fold symmetric pseudo-magnetic fields. *Nature communications* **10**, 3127, doi:10.1038/s41467-019-11038-7 (2019).

13 Villarreal, R. *et al.* Breakdown of Universal Scaling for Nanometer-Sized Bubbles in Graphene. *Nano letters* **21**, 8103-8110, doi:10.1021/acs.nanolett.1c02470 (2021).

14 Lee, C., Wei, X., Kysar, J. W. & Hone, J. Measurement of the Elastic Properties and Intrinsic Strength of Monolayer Graphene. **321**, 385-388, doi:doi:10.1126/science.1157996 (2008).

15 Castellanos-Gomez, A. *et al.* Elastic Properties of Freely Suspended MoS2 Nanosheets. *Adv. Mater.* **24**, 772-+, doi:10.1002/adma.201103965 (2012).

16 Cao, G. Atomistic Studies of Mechanical Properties of Graphene. **6**, 2404-2432 (2014).

17 Maali, A., Cohen-Bouhacina, T., Couturier, G. & Aime, J. P. Oscillatory dissipation of a simple confined liquid. *Physical review letters* **96**, 086105, doi:10.1103/PhysRevLett.96.086105 (2006).

18 Maali, A. *et al.* in *Applied Scanning Probe Methods XII: Characterization* (eds Bharat Bhushan & Harald Fuchs) 149-164 (Springer Berlin Heidelberg, 2009).

19 Guriyanova, S., Mairanovsky, V. G. & Bonaccurso, E. Superviscosity and electroviscous effects at an electrode/aqueous electrolyte interface: an atomic force microscope study. *J Colloid Interface Sci* **360**, 800-804, doi:10.1016/j.jcis.2011.04.072 (2011).